

Citation for published version:

Gao, J, Zang, J, Chen, L, Chen, Q, Ding, H & Liu, Y 2019, 'On hydrodynamic characteristics of gap resonance between two fixed bodies in close proximity', *Ocean Engineering*, vol. 173, pp. 28-44.
<https://doi.org/10.1016/j.oceaneng.2018.12.052>

DOI:

[10.1016/j.oceaneng.2018.12.052](https://doi.org/10.1016/j.oceaneng.2018.12.052)

Publication date:

2019

Document Version

Peer reviewed version

[Link to publication](#)

Publisher Rights

CC BY-NC-ND

University of Bath

General rights

Copyright and moral rights for the publications made accessible in the public portal are retained by the authors and/or other copyright owners and it is a condition of accessing publications that users recognise and abide by the legal requirements associated with these rights.

Take down policy

If you believe that this document breaches copyright please contact us providing details, and we will remove access to the work immediately and investigate your claim.

1 On hydrodynamic characteristics of gap resonance between two fixed bodies in close
2 proximity

3 Junliang Gao^{1,2}, Jun Zang^{2*}, Lifan Chen³, Qiang Chen², Haoyu Ding², Yingyi Liu⁴

4 1 School of Naval Architecture and Ocean Engineering, Jiangsu University of Science and
5 Technology, Zhenjiang 212003, China

6 2. Research Unit for Water, Environment and Infrastructure Resilience (WEIR), Department of
7 Architecture and Civil Engineering, University of Bath, BA2 7AY, U.K.

8 3. Faculty of Engineering and Mathematical Sciences, University of Western Australia, Crawley
9 WA6009, Australia

10 4. Research Institute for Applied Mechanics, Kyushu University, Kasuga, Fukuoka 816-8580,
11 Japan

12
13 **Abstract:**

14 The resonant water motion inside a narrow gap between two identical fixed boxes that are in
15 side-by-side configuration is investigated using a two-dimensional (2D) numerical wave tank based
16 on OpenFOAM[®], an open source CFD package. Gap resonance is excited by regular waves with
17 various wave heights, ranging from linear waves to strong nonlinear waves. This paper mainly
18 focuses on the harmonic analyses of the free-surface elevation in the narrow gap and wave loads
19 (including the horizontal wave forces, the vertical wave forces and the moments) on the bodies. It
20 is found that the influences of the incident wave height on the higher-order harmonic components
21 of different physical quantities are quite different. The effects of the incident wave height on the
22 reflection, transmission and energy loss coefficients are also discussed. Finally, aiming at the
23 quantitative estimation of the response time and the damping time of gap resonance, two different
24 methods are proposed and verified for the first time on gap resonance.

25
26 **Keywords:** Gap resonance; Wave height amplification; Wave force; Harmonic analysis; Response
27 time and damping time of gap resonance; OpenFOAM[®]

28

* Corresponding author. E-mail: J.Zang@bath.ac.uk.

29 1. Introduction

30 In the past few decades, as the oil and gas industry have moved towards deeper waters and
31 harsher environments, Floating Production Storage and Offloading (FPSO) platforms have shown
32 great potential as the most economic ways to process and distribute the hydrocarbon products. One
33 of the key challenges for FPSO platforms lies in the safe offloading operations from them to a shuttle
34 tanker when the tanker is positioned side-by-side with them. When multiple floating bodies are
35 deployed side-by-side in close proximity and are subjected to incident water waves, drastic water
36 surface oscillations may occur inside the narrow gaps between them at certain frequencies. This
37 phenomenon is normally referred to as “gap resonance”.

38 The hydrodynamic interactions of multiple bodies with narrow gaps between have been
39 investigated extensively due to its relevance to offloading facilities for FPSO. The methods used in
40 these studies include theoretical analyses, physical experiments and numerical simulations. The
41 theoretical analyses were mainly used in the early studies of the gap resonance problem and were
42 mainly based on the linear potential flow theory (Miao et al., 2000; Molin, 2001). Subsequently, to
43 better understand gap resonance and to validate the theoretical analyses, a large number of physical
44 model tests in 2D and 3D wave basins were also implemented by previous researchers (e.g., Iwata
45 et al. (2007); Saitoh et al. (2006); Zhao et al. (2017)). The numerical investigations conducted so far
46 are mainly based on the classical potential flow model employing the boundary element method and
47 scaled boundary finite element method (e.g., Li et al. (2005); Li and Zhang (2016); Sun et al. (2010)).

48 Although both theoretical analyses and the numerical simulations based on the potential flow
49 theory have been shown to predict the resonant frequency well, they were reported to significantly
50 over-estimate the resonant wave height inside the gap and the wave forces on the floating bodies,
51 because the physical energy dissipation due to the fluid viscosity, vortex shedding and even
52 turbulences cannot be considered in the context of potential flow theory. To overcome this problem,
53 several particular numerical techniques that artificially introduce wave energy dissipation term into
54 the potential flow model were developed so far (Chen, 2004; Huijsmans et al., 2001; Lu et al., 2010b;
55 Newman, 2004; Ning et al., 2015a, b). However, the introduction of artificial damping term seems
56 somewhat arbitrary for the rigorous potential theory, and under some conditions it was found to be
57 difficult to obtain a unique value of the damping parameter (Pauw et al., 2007; Tan et al., 2014). In
58 recent years, with the fast developments of computing technology, the CFD simulation has gradually

59 become an alternative method in investigating the gap resonance problem (Jiang et al. (2018); Lu et
60 al. (2010a); Lu et al. (2011a); Lu et al. (2011b); Moradi et al. (2015, 2016)). All these studies found
61 that the results obtained by the CFD simulations agreed well with those from existing experiments.

62 While many research efforts into the gap resonance have been undertaken, the majority have
63 concentrated on the analyses of the overall resonant wave height in the narrow gap and the overall
64 wave loads on the boxes under the condition of the linear or weakly nonlinear regular waves (e.g.,
65 Feng et al. (2017); Jiang et al. (2018); Lu et al. (2010a); Lu et al. (2010b); Lu et al. (2011a); Lu et
66 al. (2011b); Moradi et al. (2015, 2016)). The investigations on the harmonic analyses of the wave
67 height and wave loads are relatively rare. By using a semi-analytical formulation of the velocity
68 potentials, Mavrakos and Chatjigeorgiou (2009) investigated the significance of the second-order
69 effects to the total wave loading on a cylindrical moonpool, especially in the frequency regions in
70 which the fluid resonance occurs. Sun et al. (2010) employed a 3D boundary element code
71 DIFFRACT to investigate the first- and second-order loads and free-surface elevations for two side-
72 by-side rectangular barges. However, both of their methods are based on the classical potential flow
73 theory which does not consider the physical energy dissipation due to the viscous effect. Hence,
74 some of their findings may not reflect real phenomena of the fluid resonance in the narrow gap or
75 in the moonpool, where the physical energy dissipation plays an important role. Zhao et al. (2017)
76 investigated experimentally the first and higher harmonic components of the resonant fluid response
77 in the gap between two identical fixed rectangular boxes excited by the transient focused wave
78 groups in a 3D wave basin. However, the gap resonance induced by the regular waves and the
79 harmonic analyses on wave loads were not considered in that paper.

80 To further improve the understanding of related phenomena involved in gap resonance, this
81 paper mainly focuses on the variations of the first and higher harmonic components of free-surface
82 elevation inside the gap and wave loads on boxes with respect to the wave height of the incident
83 regular waves when gap resonance occurs. In this paper, the system of two identical boxes is taken
84 as the background of this study. For comparison, the same problem is also investigated when the
85 free-surface elevation in the narrow gap is under non-resonant conditions. Compared to the previous
86 investigations (i.e., Feng et al. (2017); Jiang et al. (2018); Lu et al. (2010a); Lu et al. (2010b); Lu et
87 al. (2011a); Lu et al. (2011b); Moradi et al. (2015, 2016)), stronger nonlinear incident waves are
88 used in this paper, which is necessary due to the fact that FPSO platforms are often exposed to severe

89 wave conditions. Subsequently, the variations of the reflection coefficient C_r , the transmission
90 coefficient C_t and the energy loss coefficient $L_e = 1 - C_r^2 - C_t^2$ with respect to the frequency of
91 the incident waves with various wave heights are also discussed, because an integral comprehension
92 of these coefficients may promote the better understanding of the mechanism essence of the gap
93 resonance (Jiang et al., 2018). Meanwhile, these previous studies were mainly concerned on the
94 related hydrodynamic phenomena after the free-surface resonance in the narrow gap reached the
95 steady state, and both the response and the damp phases were paid little attention to. In the current
96 paper, both the response time and the damping time of gap resonance are quantitatively evaluated
97 by two different methods. In practical engineering applications, the fast and accurate estimation of
98 the response time and the damping time is very important for the safe evacuation of staff and the
99 reasonable arrangement of operation time during the offloading operations from a FPSO platform
100 to a shuttle tanker under gap resonance conditions.

101 In Sections 2, 3 and 4, the numerical model employed in this work, numerical experimental
102 setup and the validations of the numerical model against available experimental and numerical data
103 are presented, respectively. The numerical results and discussions are presented in Section 5. Finally,
104 conclusions are drawn in Section 6.

105

106 2. Numerical model description

107 To consider the physical energy dissipation near the gap due to the viscous effect, a viscous
108 flow solver is necessary. In this paper, the numerical wave tank is based on the OpenFOAM®
109 multiphase solver “interFoam”, and waves are generated and dissipated using the relaxation-based
110 wave generation toolbox “waves2Foam” proposed by Jacobsen et al. (2012).

111 2.1. Governing equations

112 The continuity and Navier-Stokes equations are utilized as the governing equations to solve
113 the two-phase flow of water and air:

$$114 \quad \frac{\partial \rho}{\partial t} + \nabla \cdot (\rho \mathbf{u}) = 0, \quad (1)$$

$$115 \quad \frac{\partial \rho \mathbf{u}}{\partial t} + \nabla \cdot (\rho \mathbf{u} \mathbf{u}^T) = -\nabla P - (\mathbf{g} \cdot \mathbf{x}) \nabla \rho + \nabla \cdot (\mu \nabla \mathbf{u}) + \sigma_i k_\alpha \nabla \alpha, \quad (2)$$

116 where ρ is the fluid density, $\nabla = \left(\frac{\partial}{\partial x}, \frac{\partial}{\partial y}, \frac{\partial}{\partial z} \right)$ is the gradient operation, $\mathbf{u} = (u, v, w)$ is the velocity
117 vector of the fluid, $\mathbf{x} = (x, y, z)$ is the Cartesian coordinate vector, \mathbf{g} is the gravitational acceleration,

118 P is the pressure in excess of the hydrostatic part, μ is the dynamic viscosity of the fluid, σ_i is the
 119 surface tension coefficient and k_α is the surface curvature. The above equations are solved for
 120 both water and air simultaneously. α denotes the volume fraction of water in the computational cell,
 121 which takes a value of 1 for water and 0 for air and intermediate values for a mixture of water and
 122 air. The distribution of α is modelled by the following advection transport equation:

$$123 \quad \frac{\partial \alpha}{\partial t} + \nabla \cdot (\alpha \mathbf{u}) + \nabla \cdot [\alpha(1-\alpha)\mathbf{u}_r] = 0, \quad (3)$$

124 in which $\mathbf{u}_r = \mathbf{u}_{\text{water}} - \mathbf{u}_{\text{air}}$ is a relative velocity between the water and the air. Using α , the spatial
 125 variation of any fluid property φ (e.g., the fluid density ρ and the dynamic viscosity μ) can be
 126 expressed through the weighting

$$127 \quad \varphi = \alpha \varphi_{\text{water}} + (1-\alpha) \varphi_{\text{air}}, \quad (4)$$

128 where the subscripts “water” and “air” denote the corresponding fluid property of water and air,
 129 respectively.

130 2.2. Boundary conditions and numerical implementations

131 The toolbox “waves2Foam” proposed by [Jacobsen et al. \(2012\)](#) is employed to generate and
 132 absorb waves at the boundaries (see Fig. 1). At the inlet and the outlet boundaries, the velocities are
 133 defined as that of a regular incoming wave and as zero, respectively, and the pressure gradients are
 134 set to zero. Two relaxation zones are deployed at the inlet and the outlet boundaries to absorb the
 135 reflected and the transmitted waves. At the upper part of the tank, the boundary condition is set as
 136 “atmosphere”; while at the bottom of the tank and the solid walls of the fixed boxes, “no-slip”
 137 boundary condition is applied. For a 2D problem, the boundary condition on the walls in the third
 138 dimension is set to “empty”.

139 The governing equations (1)-(2) and the advection transport equation (3) are solved based on
 140 the finite volume method. The velocity-pressure coupling is calculated using the PISO (Pressure
 141 Implicit with Splitting of Operator) algorithm. Gradients are approximated by the Gaussian
 142 integration method based on a linear interpolation from cell centers to cell faces. The time
 143 derivatives are solved by a first-order Euler scheme. The Gauss Convection-specific schemes are
 144 used for the evaluation of the divergence terms. Identical to [Feng et al. \(2017\)](#), to produce accurate
 145 and stable results, the largest Courant number is set to 0.25 in all simulations.

146 **Once Eqs. (1)-(3) are solved at each time step, the wave force and the moment on the structure**

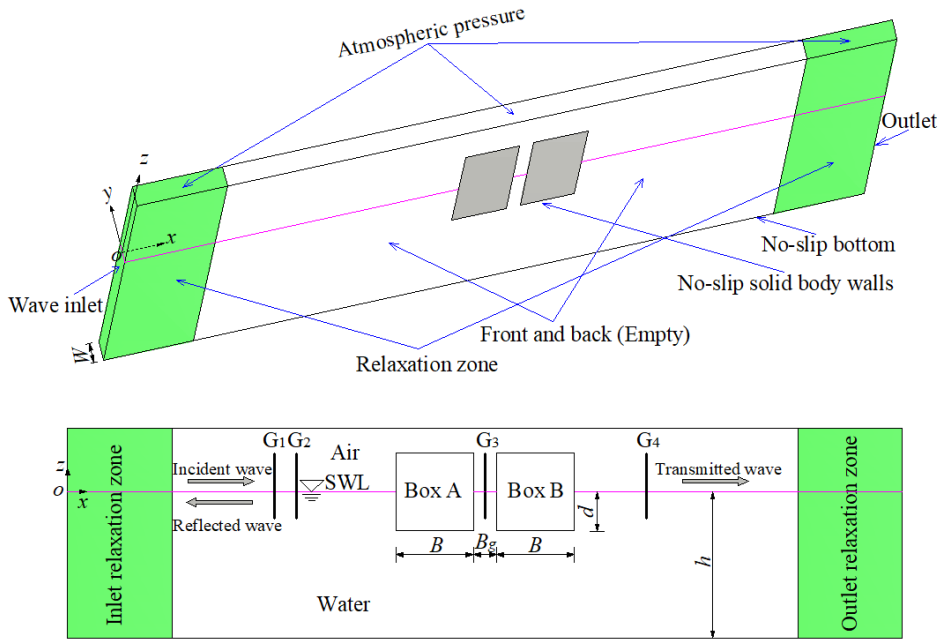
147 can be calculated by the following formulations:

$$148 \quad \mathbf{F} = \int_{\Omega} [P\mathbf{n} + \mu(\partial\mathbf{u}_{\tau}/\partial\mathbf{n})] ds, \quad (5)$$

149 and

$$150 \quad \mathbf{M} = \int_{\Omega} \mathbf{r} \times [P\mathbf{n} + \mu(\partial\mathbf{u}_{\tau}/\partial\mathbf{n})] ds, \quad (6)$$

151 where \mathbf{F} and \mathbf{M} are the vectors of the wave force and the moment, respectively, \mathbf{u}_{τ} is the tangent
 152 velocity component, \mathbf{n} is the unit normal vector, ds is the surface area differential on the wet solid
 153 surface Ω , and \mathbf{r} is the position vector of ds relative to a certain space point. For the gap resonance
 154 problem that will be described in detail in Section 3, the moments on the two fixed boxes correspond
 155 to their respective centroids. As for the harmonic analysis for various variables (i.e., the free-surface
 156 elevation in the gap, the horizontal and vertical wave forces and the moments on the two boxes),
 157 they are performed by using the discrete Fourier transform for the time-histories of their respective
 158 signals.



159
 160 **Fig. 1.** Sketch of the numerical wave tank: (a) boundary conditions and the definition of the
 161 coordinate system; (b) positions of wave gauges and the definition of the geometric parameters.

162 3. Numerical wave tank

163 Fig. 1 illustrates the sketch of the 2D numerical wave tank used in the present study. The wave
 164 tank has a length of 18.5 m, a height of 0.8 m and a width of $W=0.1$ m. The origin of the coordinate
 165 system is located at the still water level (SWL) of the left inlet boundary. The x -axis is in the wave

166 propagation direction, and the z -axis is in the upward direction. The thickness of the wave tank in
167 y -direction corresponds to a cell. Two identical fixed boxes are placed at the middle of the wave
168 tank. The box height is $H=0.5$ m, the breadth is $B=0.5$ m, the draft $d=0.25$ m, the gap width $B_g=0.05$
169 m, the water depth is $h=0.5$ m, and the air depth is $h_a=0.3$ m. This configuration is in accordance
170 with the physical experiments in [Saitoh et al. \(2006\)](#) as well as the numerical investigations in [Lu](#)
171 [et al. \(2008; 2011a; 2011b\)](#).

172 Five sets of simulations are implemented, in which the wave heights of the incident regular
173 waves are set to $H_0 = 0.010$ m, 0.024 m, 0.050 m, 0.075 m and 0.100 m, respectively. The wave
174 frequency, ω , considered in all the five sets of simulations ranges from 4.456 rad/s to 7.534 rad/s.
175 Correspondingly, the dimensionless wavenumber, kh , ranges from 1.210 to 2.910, where $k=2\pi/L$
176 denotes the wavenumber and L denotes the wavelength. Four wave gauges, G_1 - G_4 , are arranged to
177 record the free-surface elevations. G_1 and G_2 are utilized to decompose the incident and reflected
178 waves, and their distance is set to 0.25 m. G_3 and G_4 are used to obtain the free surfaces inside the
179 gap and the transmitted waves. G_3 is placed in the middle of the gap; while G_2 and G_4 are positioned
180 at 1.50 m from the left side of Box A and the right side of Box B, respectively. Two relaxation zones
181 of 5.50 m long each are placed at the inlet and outlet boundaries of the wave tank to absorb the
182 reflected and transmitted waves. The length of 5.50 m is approximately 2.11 times of the maximum
183 wavelength that corresponds to the incident waves with $\omega=4.456$ rad/s.

184 A built-in mesh generation utility supplied with OpenFOAM®, “blockMesh”, is employed to
185 generate meshes. A typical computational mesh is shown in Fig. 2. Non-uniform meshes are adopted
186 for saving the computational time. The fine meshes with higher resolution are used around the boxes,
187 especially in the vicinity of the narrow gap. To capture the interface between water and air, the
188 meshes gradually become denser from the bottom and the atmosphere boundaries to the still water
189 level.

190

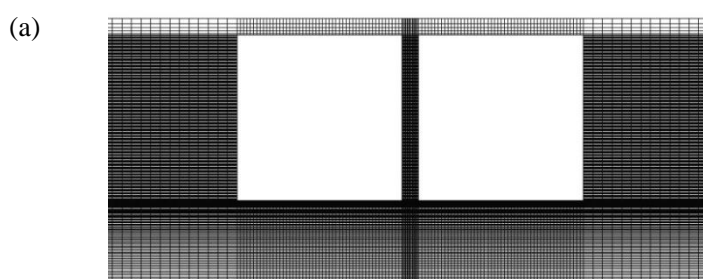
191

192

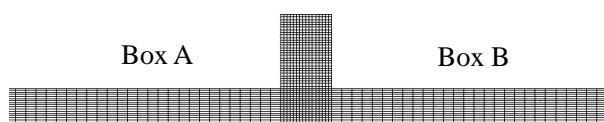
193

194

195

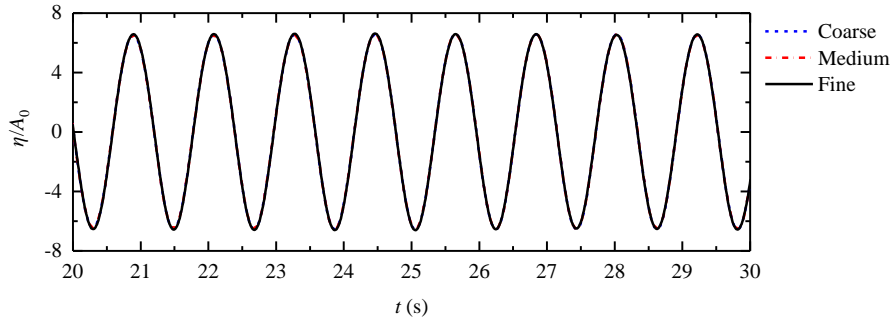


(b)



196
197
198
199
200
201
202
203
204

Fig. 2. Side view of typical meshes in the computational domain: (a) the meshes around the boxes;
(b) the meshes close to the gap inlet



205
206
207
208
209

Fig. 3. Dependence of the free-surface elevation in the gap on the mesh resolution for the incident waves with $kh=1.556$ and $H_0=0.010$ m, in which $A_0= H_0/2$ denotes the amplitude of the incident waves.

210
211
212
213
214
215
216
217
218
219
220

To examine the dependence of the numerical results on the mesh resolution, the free-surface response in the narrow gap is simulated using three different meshes, namely the coarse, medium and fine meshes. The numbers of the cells for these three meshes are 143600, 224060 and 340880, respectively. Based on the numerical results that will be shown in Section 4.1, the free-surface resonance in the gap occurs at $kh=1.556$. Fig. 3 presents the resonant free surfaces inside the gap induced by the incident waves with $kh=1.556$ and $H_0=0.010$ m. $A_0=H_0/2$ in this figure denotes the incident wave amplitude. It is seen that the time histories of the free-surface elevations for the three mesh configurations are almost identical to each other. **Meanwhile, considering that the medium mesh can provide more accurate simulations of the wave fields excited by the incident waves with higher frequencies as compared to the coarse mesh, in all our numerical simulations, the medium mesh configuration is employed.**

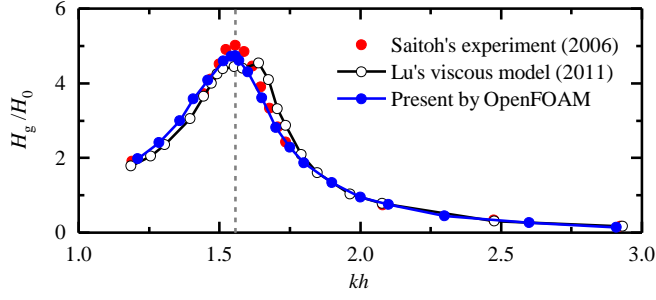
221 For most of the simulations, a total time of 40.0 s is considered. However, to study the damping
222 time of the resonant free surface, for the five cases in which the incident wave frequency equals the
223 resonant frequency, a total time of 70.0 s is employed. The wave inlet boundary stops working after
224 40.0 s, and the numerical model continues to simulate the damping process. It can be seen from Fig.
225 3 that the free-surface elevation in the gap has already reached the steady state at $t=20.0$ s. All the
226 numerical results that will be presented in Section 4.1 and Sections 5.1–5.3 are based on the simulated
227 steady-state data from 20.0 s to 40.0 s. While in Section 5.4, the time histories of the free-surface
228 elevation in the gap between 0 – 20.0 s and 40.0 s – 70.0 s are utilized to investigate the response
229 time and the damping time of gap resonance, respectively.

230

231 4. Numerical model validations

232 To guarantee the reliability of the model and the accuracy of the numerical results, the
233 numerical model and the numerical wave tank illustrated in Sections 2 and 3 are first validated by
234 comparing the present results obtained by OpenFOAM[®] with available experimental data and
235 numerical results in previous literatures. For the simulations with $H_0=0.024$ m described in Section
236 3, [Saitoh et al. \(2006\)](#) and [Lu et al. \(2011b\)](#) have measured the amplification of the free-surface
237 elevation inside the gap and the wave forces on boxes by using physical experiments and a viscous
238 flow model, respectively. Comparisons of the present results with those in the two papers will be
239 presented in Section 4.1. Because the current research mainly focuses on the harmonic analysis of
240 the free-surface elevation in the gap and the wave loads on the boxes, it is essential to further
241 examine the capability of the present model to predict the higher-order harmonic components of the
242 free-surface elevation or the wave loads. To the best of our knowledge, for the gap resonance
243 problem, the experimental data on the higher-order harmonic components of the free-surface
244 elevation or the wave loads are rare. However, [Rodríguez et al. \(2016\)](#) implemented physical
245 experiments on the interactions between regular waves and one fixed box, and the experimental data
246 of the vertical wave force on the box (including the first- and second-order harmonic components)
247 were presented in that paper. The numerical reproduction for part of their experiments will be
248 implemented in Section 4.2.

249 4.1. Two-boxes condition



250

251

Fig. 4. Amplification of the free-surface elevation inside the narrow gap for the cases with $H_0=0.024$ m, in which H_g denotes the wave height inside the narrow gap.

252

253

254

255

256

257

258

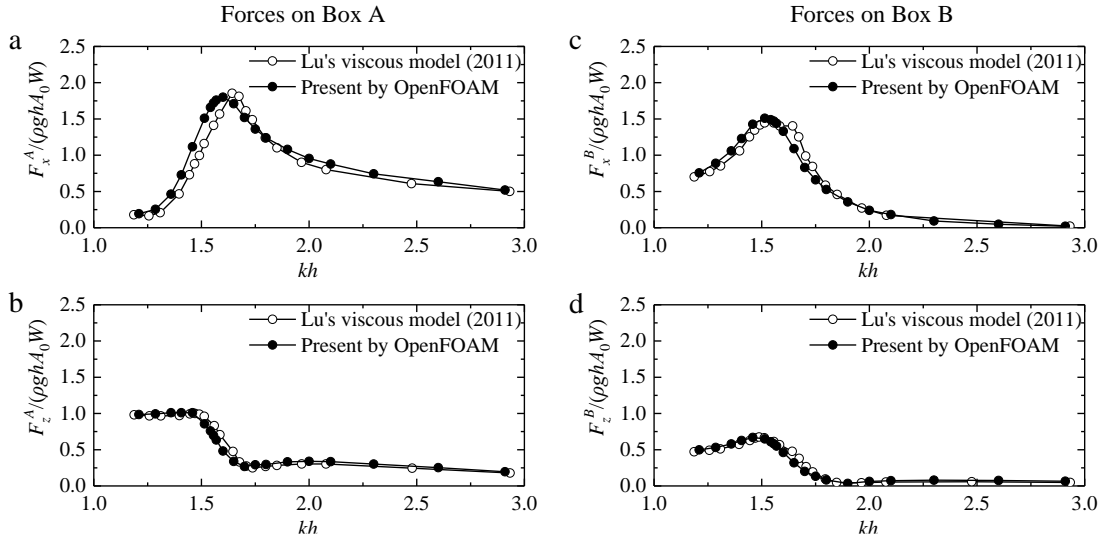
259

260

261

262

Fig. 4 illustrates the amplification of the free-surface elevation inside the narrow gap excited by the incident waves with $H_0=0.024$ m. It can be seen that the predicted resonant frequency, $kh=1.556$, by the present numerical model is almost identical to those obtained by both the laboratory tests of [Saitoh et al. \(2006\)](#) and the CFD results of [Lu et al. \(2011b\)](#). Besides, in general, the variation of H_g/H_0 with respect to kh also agrees well with their results. Fig. 5 further presents the comparisons of the horizontal and vertical wave forces on Boxes A and B predicted by OpenFOAM® and those by the CFD results in [Lu et al. \(2011b\)](#). Similar to Fig. 4, the overall agreement between the present results and those in [Lu et al. \(2011b\)](#) is also observed.



263

264

Fig. 5. Variations of the wave forces on the two boxes with respect to the incident wave frequency.

265

(a) and (b) correspond to the horizontal and vertical forces on Box A, respectively; (c) and (d)

266

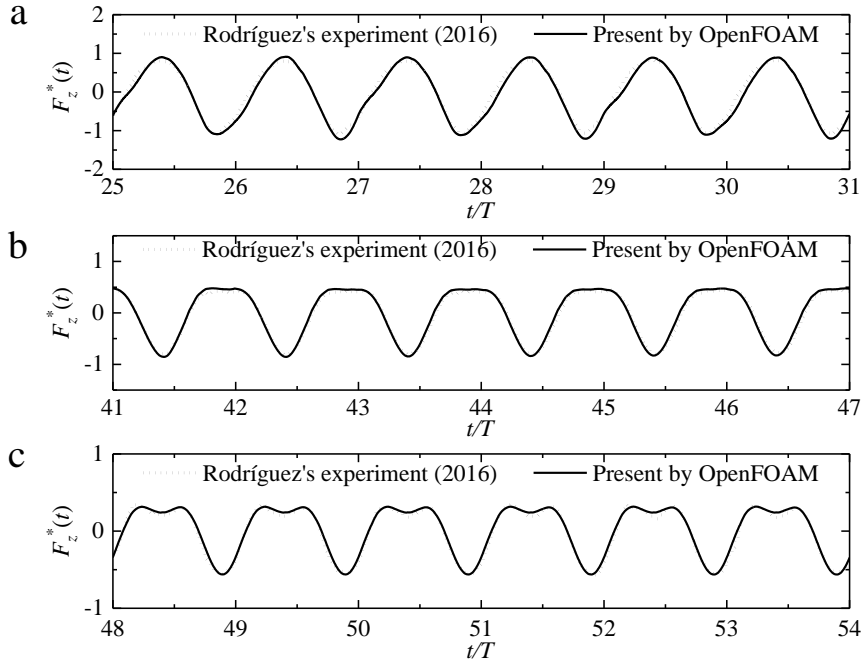
correspond to the horizontal and vertical forces on Box B, respectively.

267

268 4.2. One-box condition

269 [Rodríguez et al. \(2016\)](#) performed laboratory experiments in a 2.79 m wide and 63.00 m long
270 wave tank, and the water depth is $h=1.25$ m. A rectangular box was placed approximately in the
271 center of the wave tank, at $x=29$ m, where $x=0$ defines the location of the wave-maker. Because the
272 experimental study sought to achieve 2D flow conditions, the width of the rectangular box was
273 chosen as 2.76m, leaving only a very small gap of 0.015 m to either of the tank's sidewalls. Single
274 box geometry with the breadth $B=0.50$ m and the draught $d=0.25$ m. The regular incident waves
275 with $0.4 \leq kB \leq 2.4$ were considered. Two series of physical experiments were carried out with two
276 steepnesses of the incident waves $kA_0 = 0.05$ and 0.10. To examine the performance of the numerical
277 model for the strongly nonlinear wave conditions, the series of experiments with $kA_0 = 0.10$ are
278 reproduced by OpenFOAM® here. Considering that the box used in [Rodríguez et al. \(2016\)](#) has the
279 same breadth and draft with the two boxes shown in Fig. 1, a very similar numerical wave tank (not
280 shown in this paper for brevity) with that in Fig. 1 is employed to implement the present simulations.
281 Compared to the wave tank shown in Fig. 1, there only exist two main differences in the present
282 wave tank. First, there is only a single box located in the middle of the present wave tank. Second,
283 the water depth is deepened from 0.50 m to 1.25 m. A mesh configuration that has a similar mesh
284 density with the medium mesh described in Section 3 is utilized. It should be noted that due to the
285 relaxation zone deployed around the inlet and outlet boundaries, it is not necessary for the numerical
286 wave tank to set the same length, 63.00 m, as the physical wave tank, and the numerical tank with
287 a length of 18.5 m is already long enough.

288 Fig. 6 presents the simulated and experimental time-histories of the non-dimensional vertical
289 wave force, $F_z(t)/(0.5\rho gA_0BW)$, for three cases with $kB=0.8, 1.4,$ and 2.0. It can be obviously seen
290 that significant nonlinearities are present, particularly for $kB=1.4$ and 2.0, due to the vertical
291 asymmetry of the force traces. Overall, the agreement between the present numerical results and the
292 experimental data is good. Fig. 7 further quantitatively compares the first- and second-order
293 harmonic components of the experimental and numerical vertical forces for all cases with $kA_0=0.10$.
294 Good agreement between the experimental and numerical results is also observed.



295

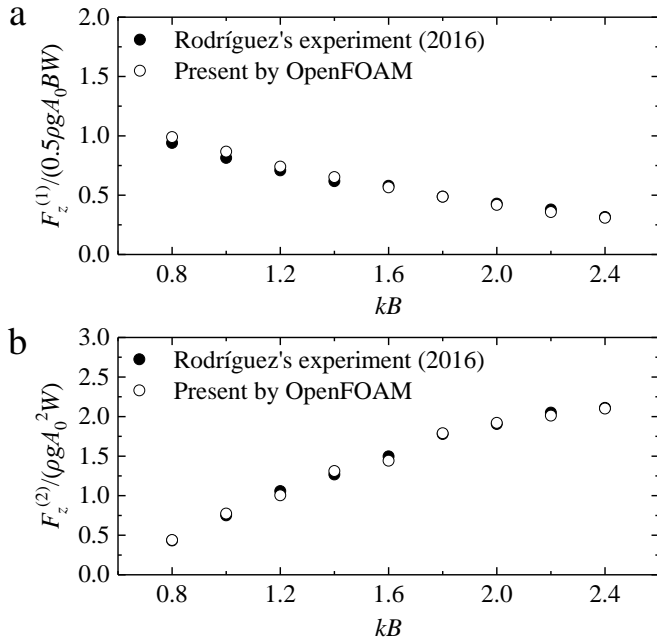
296

297

298

299

Fig. 6. Time histories of the vertical wave forces excited by the regular waves with $kA_0=0.10$ and (a) $kB=0.8$, (b) $kB=1.4$ and (c) $kB=2.0$, in which $F_z^*(t) = F_z(t)/(0.5\rho gA_0BW)$ denotes the time history of the non-dimensional vertical wave forces.



300

301

302

303

304

Fig. 7. Non-dimensional (a) first-order and (b) second-order vertical wave forces excited by the incident regular waves with $kA_0=0.10$

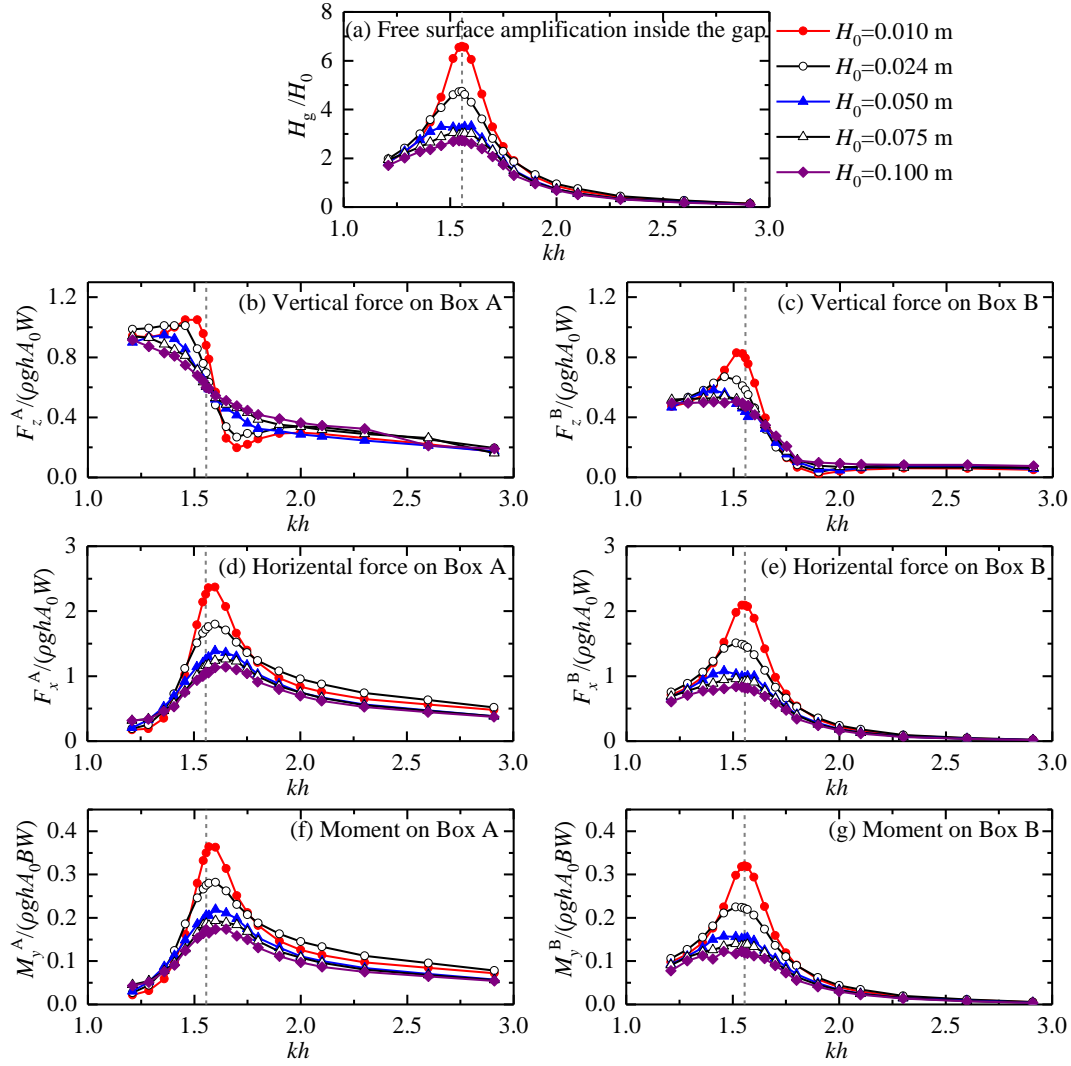
305 5. Numerical results and discussion

306 In order to present an overall impression of the hydrodynamic characteristics of gap resonance
307 under the conditions of various incident wave heights on the reader, the variations of the overall
308 wave height amplification in the narrow gap and the overall wave loads on boxes with respect to the
309 incident wave frequency are first illustrated and discussed in Section 5.1. Subsequently, to find out
310 the relative importance of different harmonic components, the first three order harmonic
311 components of the free-surface elevation in the narrow gap and the wave loads on boxes are
312 analyzed in Section 5.2. Then, to better explain some phenomena presented in Sections 5.1 and 5.2
313 and better understand the mechanism essence of gap resonance, the variations of the reflection,
314 transmission and energy loss coefficients with respect to the frequency of the incident waves with
315 various wave heights are discussed in Section 5.3. Finally, considering the importance of the fast
316 and accurate estimation of the response time and the damping time of gap resonance, two different
317 estimation methods are proposed and verified in Section 5.4.

318

319 5.1 Overall wave height amplifications and overall wave loads

320 Fig. 8 shows the overall free-surface amplification in the narrow gap and the overall wave
321 forces and moments impacting on Boxes A and B excited by the incident regular waves with various
322 wave heights. Four obvious phenomena can be easily seen. First, it is seen from Fig. 8a that the
323 resonant frequency seems not sensitive to the incident wave height. For the cases with $H_0=0.010$ m,
324 0.024 m and 0.100 m, all the three variation curves of the free-surface amplification with the
325 frequency present perfect single-peak shapes, and the maximum free-surface amplification in the
326 narrow gap always occurs at the resonant frequency, i.e., $kh=1.556$. However, for the cases with
327 $H_0=0.050$ m and 0.075 m, the two variation curves of the free-surface amplification do not show the
328 perfect single-peak shape. The two curves around the resonant frequency become flat, and the values
329 of free-surface amplification at $kh=1.556$ are even slightly less than the ones at its both adjacent
330 sides. The reason for this phenomenon can be attributed to the almost invariable reflection
331 coefficients around the resonant frequency under the conditions of $H_0=0.050$ m and 0.075 m (it will
332 be shown in Section 5.3).



333

334

Fig. 8. The overall free surface amplification in the gap and the overall wave forces and moments on Boxes A and B induced by the incident regular waves with various wave heights. The vertical dash line refers to the position of the resonant frequency.

335

336

337

338

339

340

341

342

343

344

345

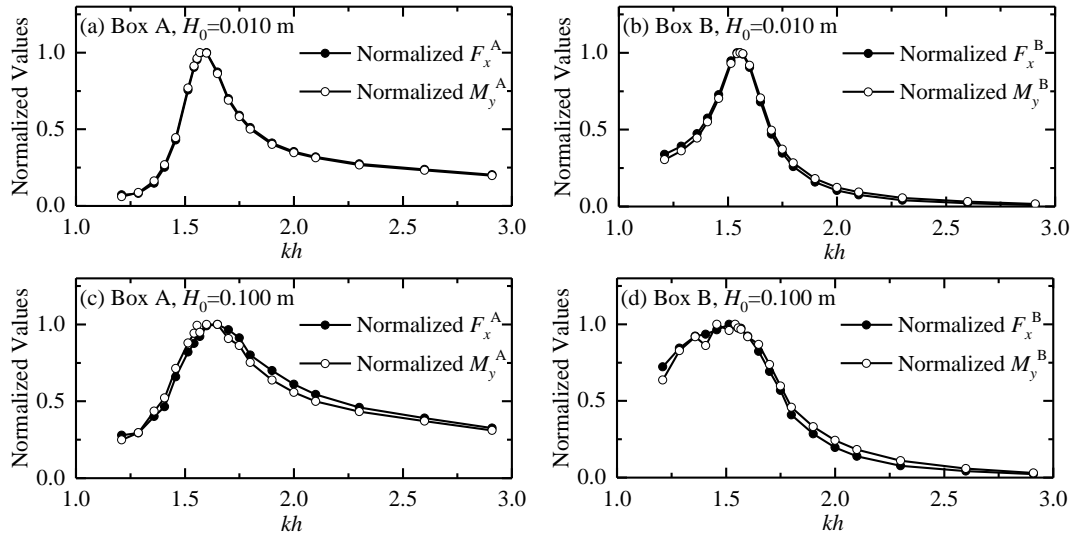
Second, for the vertical wave forces on both the two boxes (Fig. 8b and c), there exist obvious deviations between the frequency at which the maximum vertical wave force appears and the resonant frequency. However, there are some different features for the changing trends of the vertical wave forces on the two boxes. For Box A, the difference between the frequency at which the maximum vertical wave force appears and the resonant frequency monotonously increases with the incident wave height. Besides, the vertical wave forces excited by the incident wave with small height tends to increase first, then sharply decrease, then slowly increase, and then slowly decrease with the non-dimensional wavenumber, kh . However, with the increase of the incident wave height,

346 the vertical wave forces gradually become monotonic decrease with kh . For Box B, when the
347 incident wave height is small, the changing trend of the vertical wave forces with kh is similar to
348 that for Box A. When the incident wave height becomes large, the value of the vertical wave force
349 seems insensible to the incident wave frequency at the ranges of $kh < 1.5$ and $kh > 1.9$, and its value
350 only decreases sharply with the incident wave frequency at the range of $1.5 < kh < 1.9$.

351 Third, for the horizontal wave forces on Box A (Fig. 8d), the frequency at which the maximum
352 horizontal force occurs is obviously larger than the resonant frequency; the larger the incident wave
353 height is, the more obvious the deviation becomes. While for the horizontal wave forces on Box B
354 (Fig. 8e), the frequency at which the maximum horizontal force occurs is equal to or just slightly
355 less than the resonant frequency. It is due to the fact that the magnitude of the horizontal force is
356 determined by the free-surface elevation difference between the opposite sides of the each box (Lu
357 et al., 2011b). The free-surface elevation at the left side of Box A is much larger than that at the right
358 side of Box B. It leads to that the free-surface elevation difference between the opposite sides of
359 Box A is more different from the free-surface elevation in the gap, while the free-surface elevation
360 difference between the opposite sides of Box B is more close to the free-surface elevation in the gap.
361 As for the reason why the free-surface elevation at the left side of Box A is much larger than that at
362 the right side of Box B, there are two main reasons: (1) the reflected wave height is always larger
363 than the transmitted wave height (i.e., $C_r > C_t$, which will be shown in Section 5.3), and (2) the left
364 side of Box A locates at a antinode of the partially standing waves composed of the incident and the
365 reflected waves, which causes the wave height at the left side of Box A is approximately equal to
366 the summation of the incident and the reflected wave heights.

367 Fourth, for the moments on Boxes A and B (Fig. 8f and g), for all the incident wave heights
368 considered in this paper, the variation curves of the moment on each box with the frequency is very
369 similar to those of the horizontal force on the corresponding box. Hence, the phenomena described
370 above for the horizontal forces are also applicable for the moments. To further examine the
371 phenomenon that the variation curves of the moment on each box with the frequency are very similar
372 to those of the horizontal force on the corresponding box for all the incident wave heights studied
373 in this paper, Fig. 9 presents the comparisons of the normalized curves of the horizontal forces and
374 the moments on Boxes A and B for $H_0=0.010$ m and 0.100 m. The normalized curve refers to the
375 original variation curve divided by the corresponding peak value of the original variation curve.

376 Hence, the normalized curve always has a maximum value, 1.0. It can be seen that for both the two
 377 boxes and for both the two incident wave heights, the normalized curves of the horizontal wave
 378 forces are almost identical to those of the moments. For the other three incident wave heights (i.e.,
 379 $H_0=0.024$ m, 0.050 m and 0.075 m), the similar phenomenon can also be clearly observed (their
 380 comparisons are not shown in the paper for brevity).
 381



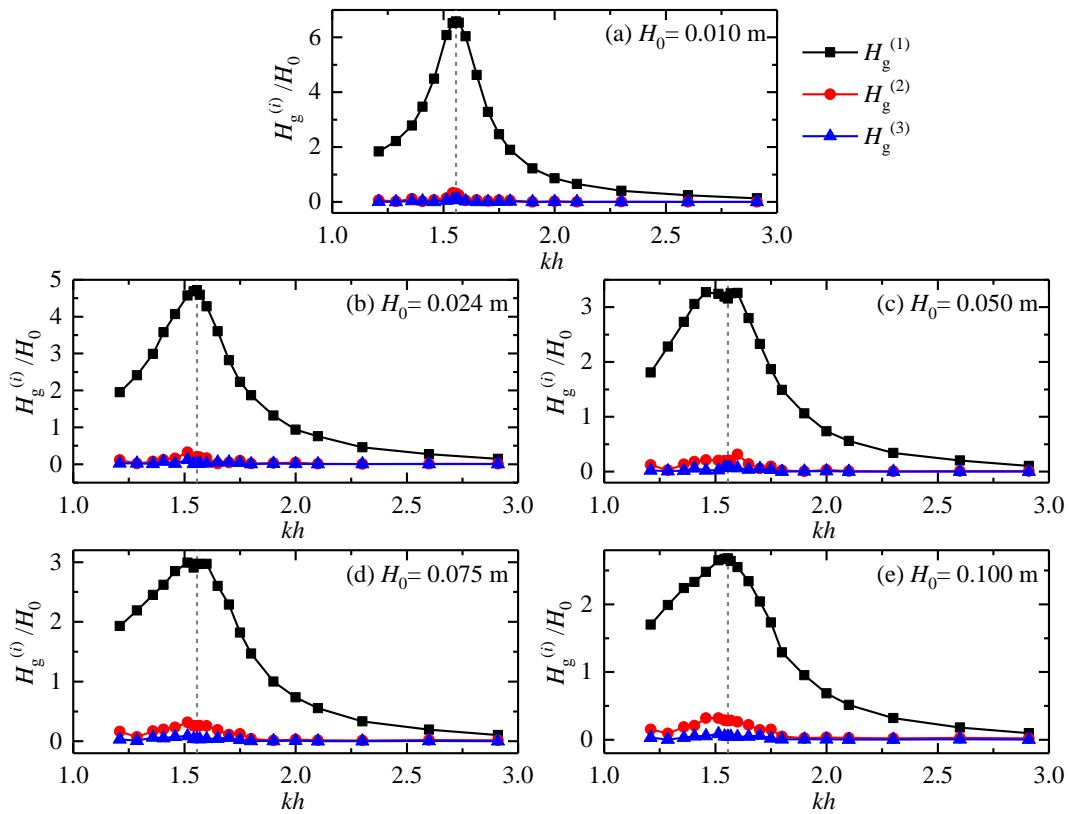
382
 383 **Fig. 9.** Comparisons of the normalized curves of the horizontal wave forces and the moments on
 384 Boxes A and B

385 5.2 Harmonic analyses of wave height amplifications and wave loads

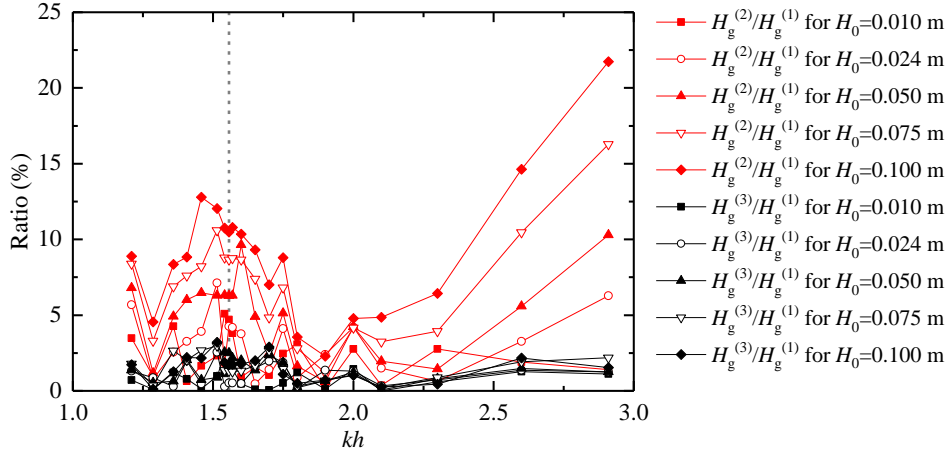
386 Fig. 10 illustrates the variation of the first three order harmonic components of the free-surface
 387 elevation in the gap with respect to the frequency under the conditions of various incident wave
 388 heights. $H_g^{(i)}$ ($i=1, 2$ and 3) in the figure denotes the i^{th} -order harmonic component of the free-surface
 389 elevation in the gap. The following three phenomena can be easily observed. First, the first-order
 390 component of the free-surface elevation is significantly larger than the second- and third-order
 391 components. Second, around the resonant frequency, the second-order component is larger than the
 392 corresponding third-order one; the larger the incident wave height is, the more obvious the
 393 phenomenon becomes. Third, all the first three order harmonic components around the resonant
 394 frequency are remarkably larger than the corresponding ones for the non-resonant conditions.

395 To quantify the relative importance of higher-order components to the first-order component,
 396 Fig. 11 further shows the ratios of the second- and third-order harmonic components to the first-
 397 order harmonic components for the free-surface elevation in the gap under the conditions of various

398 incident wave heights. It is seen that at the range of $1.3 < kh < 1.9$, there existing obvious peak points
 399 around the resonant frequency for both the second- and third-order harmonic components. For the
 400 second-order harmonic components, the maximum of their ratios to the first-order harmonic
 401 components reaches up to about 13%. It can be attributed to the fact that the free-surface elevation
 402 around the resonant frequency is remarkably amplified, and naturally the higher-order harmonic
 403 components of the free-surface elevation are enhanced due to the wave nonlinearity. While at the
 404 ranges of $kh < 1.3$ and $kh > 1.9$, as the wave frequency becomes far from the resonant frequency, the
 405 ratios of the second- and third-order components to the first-order components tend to gradually
 406 increase. It is mainly due to that the value of the first-order component significantly decreases as
 407 the wave frequency becomes far from the resonant frequency, especially for the high-frequency
 408 range (i.e., $kh > 1.9$).



409
 410 **Fig. 10.** The first three order harmonic components of the free-surface elevation in the gap under
 411 the conditions of various incident wave heights



412

413

414

415

416

417

418

419

420

421

422

423

424

425

426

427

428

429

430

431

432

433

434

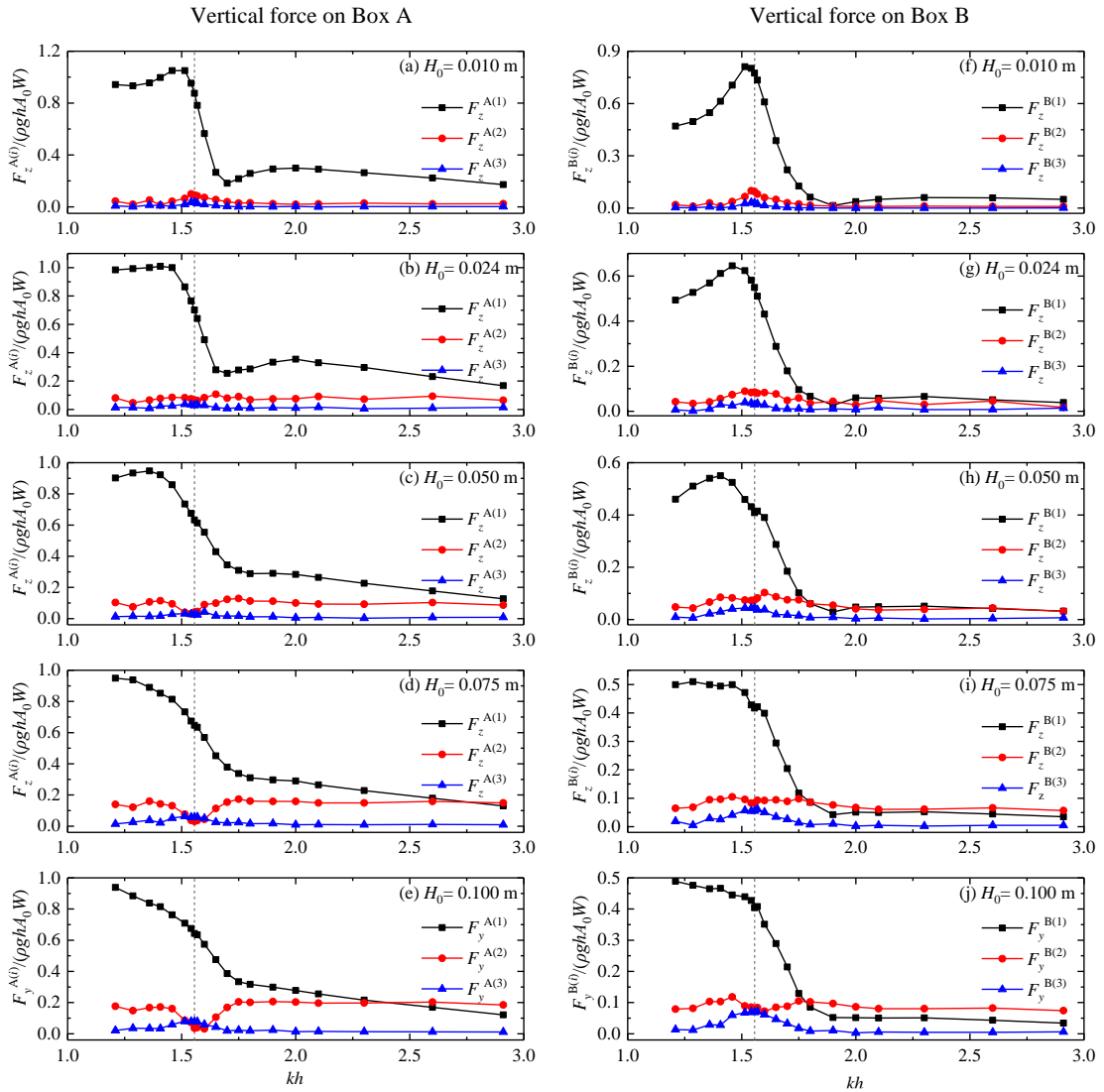
Fig. 11. Ratios of the second- and third-order harmonic components to the first-order harmonic components for the free-surface elevation in the gap under the conditions of various incident wave heights

Fig. 12 illustrates the first three order harmonic components of the vertical wave forces on Boxes A and B for all the simulations. $F_z^{A(i)}$ and $F_z^{B(i)}$ ($i=1, 2$ and 3) in this figure refer to the i^{th} -order harmonic components of the vertical wave forces on Boxes A and B, respectively. The following three phenomena can be easily seen. First, the first-order harmonic components of the vertical wave force are much larger than the higher-order components near the resonant frequency. Second, when the incident wave height is small (Fig. 12a and f), the second-order harmonic component is obviously larger than the third-order ones around the resonant frequency. As the incident wave height increases, the third-order harmonic components around the resonant frequency gradually become obviously larger than those far away from the resonant frequency; on the contrary, the second-order harmonic components around the resonant frequency become smaller and smaller compared with those far away from the resonant frequency. When the incident wave height increases up to $H_0=0.100$ m (Fig. 12e and j), the third-order harmonic components have approached (for Box B) or even exceeded (for Box A) the second-order ones. Third, for the high-frequency range, because the first-order harmonic components decrease sharply with the wave frequency, the second-order harmonic components approach and even exceed the corresponding first-order ones for both the two boxes.

Fig. 13 further shows the ratios of the second- and third-order harmonic components to the first-order harmonic components for the vertical wave forces on the two boxes for all the simulations.

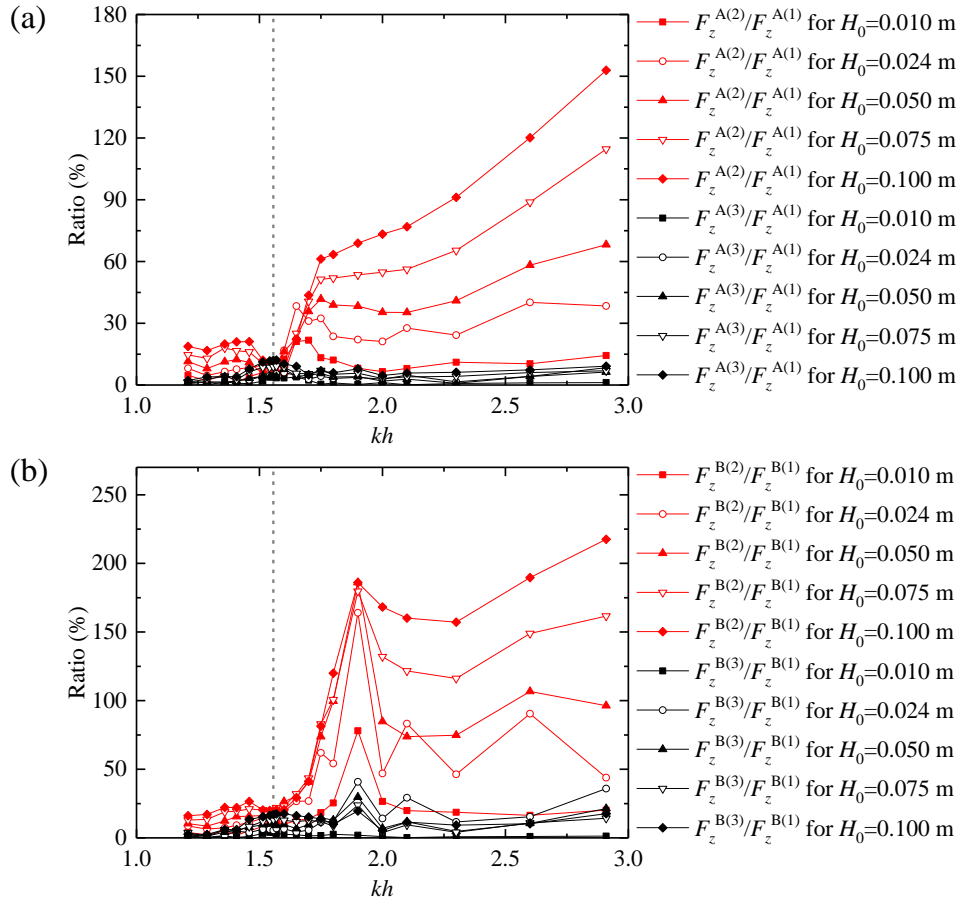
435 It can be easily observed that for both the two boxes and for the wave frequency far away from the
 436 resonant frequency, the ratio of the second- to the first-order components is always larger than the
 437 ratio of the third- to the first-order components, while around the resonant frequency, the latter
 438 approaches or even exceeds the former. Besides, for the second-order components, their ratios near
 439 the resonant frequency are less than those far from the resonant frequency. While for the third-order
 440 components, their ratios near the resonant frequency tend to be larger than those far from the
 441 resonant frequency (it is valid for the whole frequency range considered in this paper for Box A,
 442 and for $kh < 1.800$ for Box B).

443



444

445 **Fig. 12.** The first three order harmonic components of the vertical wave forces on Boxes A and B
 446 under the conditions of various incident wave heights.



447
448
449
450
451

Fig. 13. Ratios of the second- and third-order harmonic components to the first-order harmonic components for the vertical wave forces on (a) Box A and (b) Box B under the conditions of various incident wave heights

452
453
454
455
456
457
458
459
460

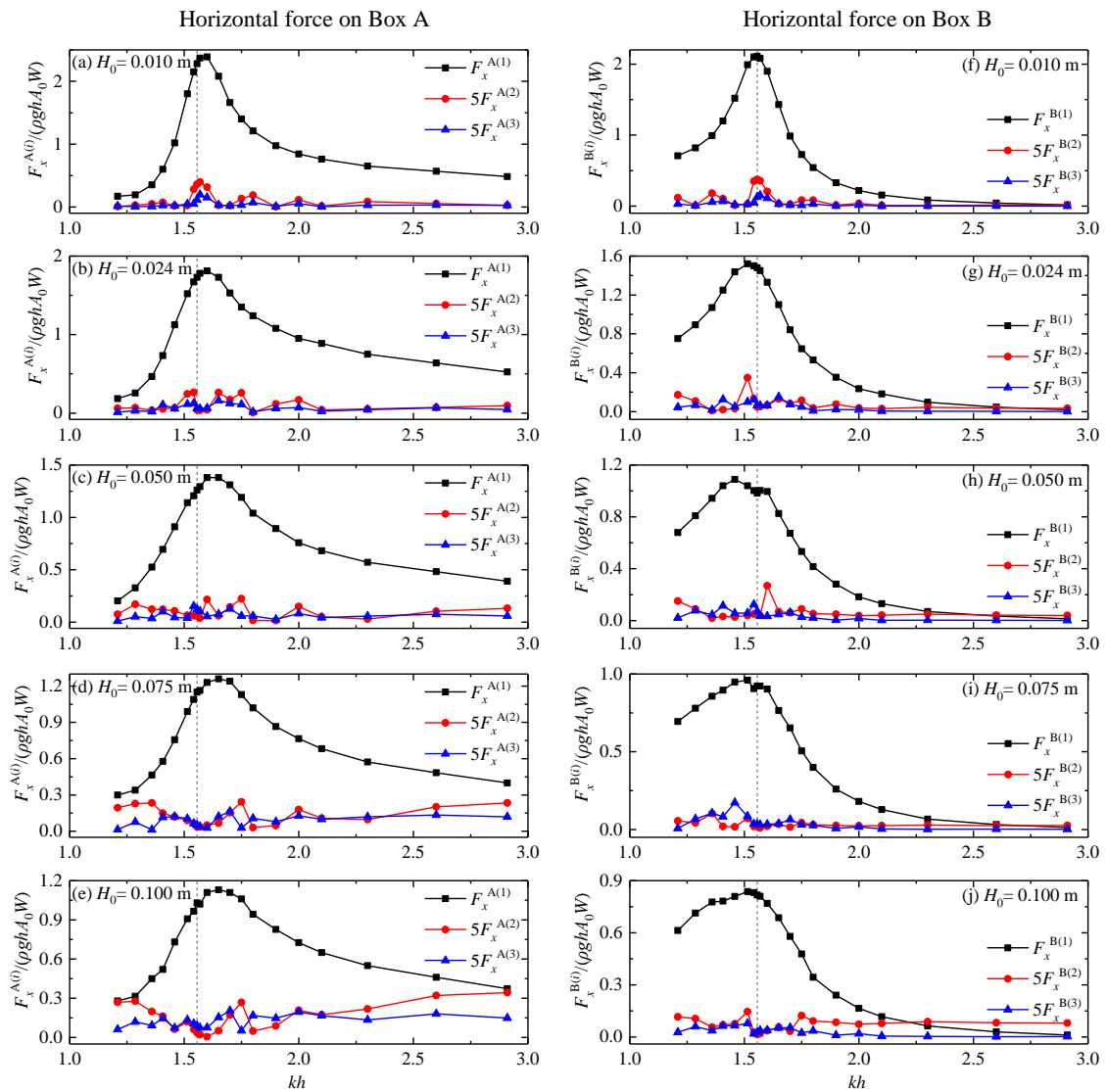
Fig. 14 presents the first three order harmonic components of the horizontal wave forces on Boxes A and B for all the simulations. $F_x^{A(i)}$ and $F_x^{B(i)}$ ($i=1, 2$ and 3) in this figure refer to the i^{th} -order harmonic components of the horizontal wave forces on Boxes A and B, respectively. Because both the second- and third-order harmonic components of the horizontal wave forces around the resonant frequency are extremely small compared to the corresponding first-order components, in order to better show the variations of all these three harmonic components with the incident wave frequency, the values of both the second- and third-order harmonic components shown in this figure are enlarged five times. In general, the above three phenomena for the vertical wave forces shown in Fig. 12 can also be observed in this figure.

461
462

Fig. 15 further presents the ratios of the second- and third-order harmonic components to the first-order harmonic components for the horizontal wave forces on the two boxes for all the

463 simulations. It should be noted that, for Box B (Fig. 15b), when $kh=2.910$ and $H_0=0.100$ m, the
 464 value of $F_x^{B(2)}/F_x^{B(1)}$ has already exceeded 140%. However, to better show the variation
 465 characteristics of the ratios around the resonant frequency, the maximum changing range of the y-
 466 axis is only set to 20%. Again, in general, all the phenomena for the vertical wave forces presented
 467 in Fig. 13 can also be observed in this figure, except that the ratios of the third- to the first-order
 468 components near the resonant frequency shown in this figure tend to be smaller than those far from
 469 the resonant frequency.

470



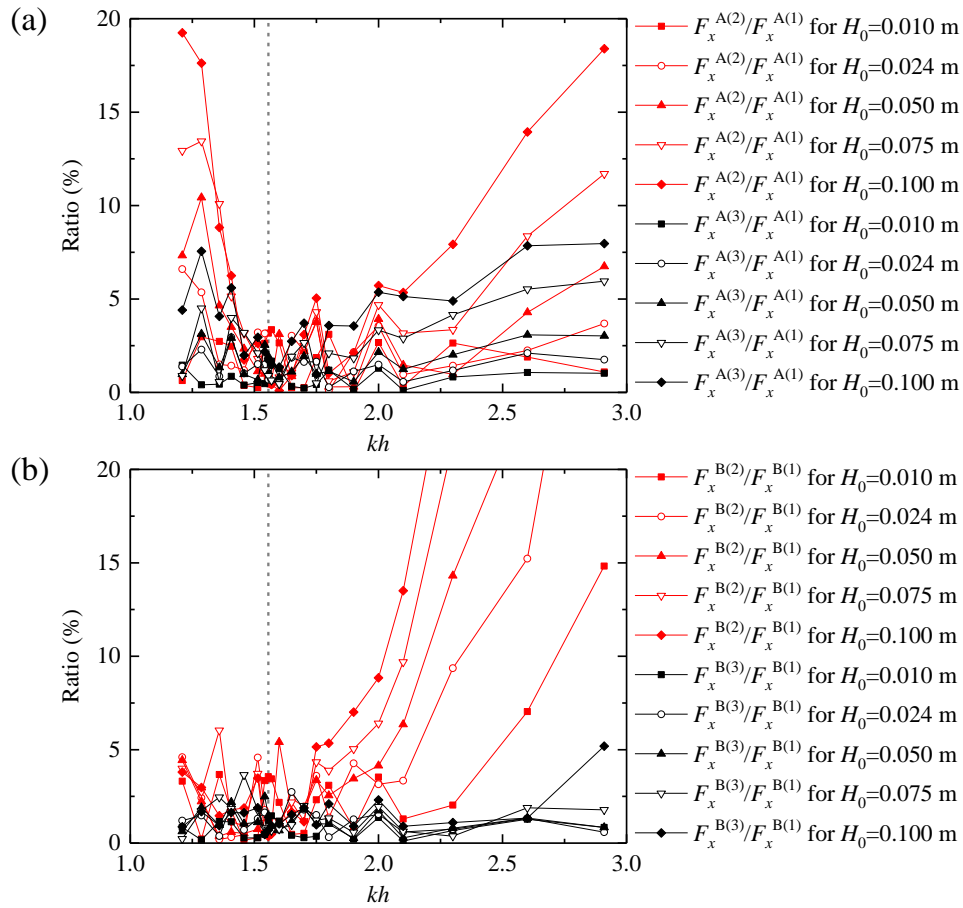
471

472 **Fig. 14.** The first three order harmonic components of the horizontal wave forces on Boxes A and

473

Box B under the conditions of various incident wave heights.

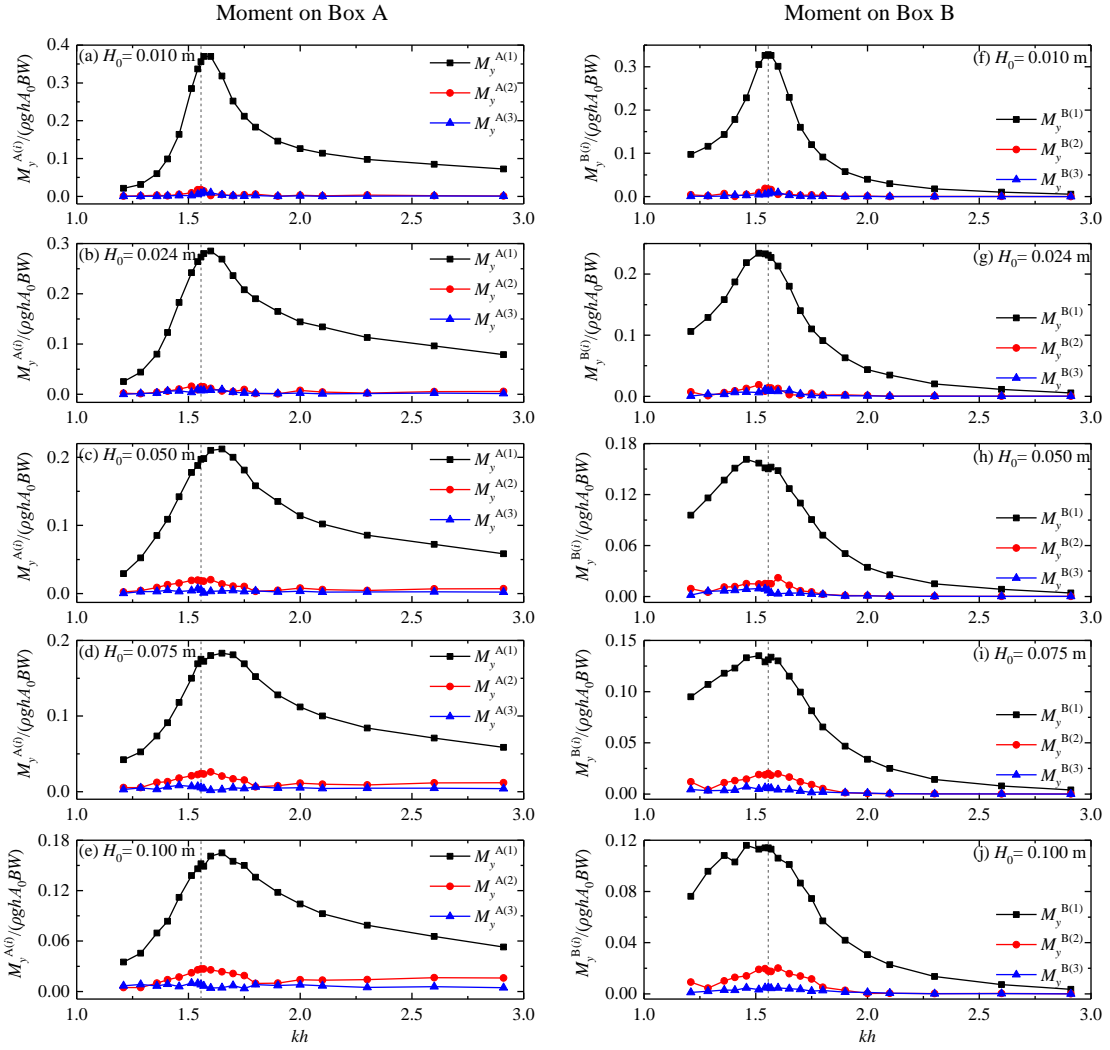
474



475
 476
 477
 478
 479
 480
 481
 482
 483
 484
 485
 486
 487
 488
 489
 490

Fig. 15. Ratios of the second- and third-order harmonic components to the first-order harmonic components for the horizontal wave forces on (a) Box A and (b) Box B under the conditions of various incident wave heights

491 Fig. 16 presents the first three order harmonic components of the moments on Boxes A and B
492 for all the simulations, in which $M_y^{A(i)}$ and $M_y^{B(i)}$ ($i=1, 2$ and 3) refer to the i^{th} -order harmonic
493 components of the moments on Boxes A and B, respectively. It is obviously seen that when the
494 incident wave height is small (refer to Fig. 16a and f), both the second- and third-order harmonic
495 components are much smaller than the corresponding first-order ones around the resonant frequency
496 for both the two boxes. However, as the incident wave height increases, the values of the second-
497 order harmonic components around the resonant frequency gradually increase. Compared to the
498 first-order harmonic components, the second-order harmonic components have reached a
499 considerable values when $H_0=0.100$ m (refer to Fig. 16e and j). To better illustrate this point, the
500 ratios of the second- and third-order harmonic components to the first-order harmonic components
501 for the moments on both the two boxes under the conditions of various incident wave heights are
502 presented in Fig. 17. It can be seen that when the incident wave height is small (i.e., $H_0=0.010$ m),
503 both the values of $M_y^{A(2)} / M_y^{A(1)}$ and $M_y^{B(2)} / M_y^{B(1)}$ are approximately 5%. However, when the
504 incident wave height increases to $H_0=0.100$ m, both their values reach up to near 20%.



505

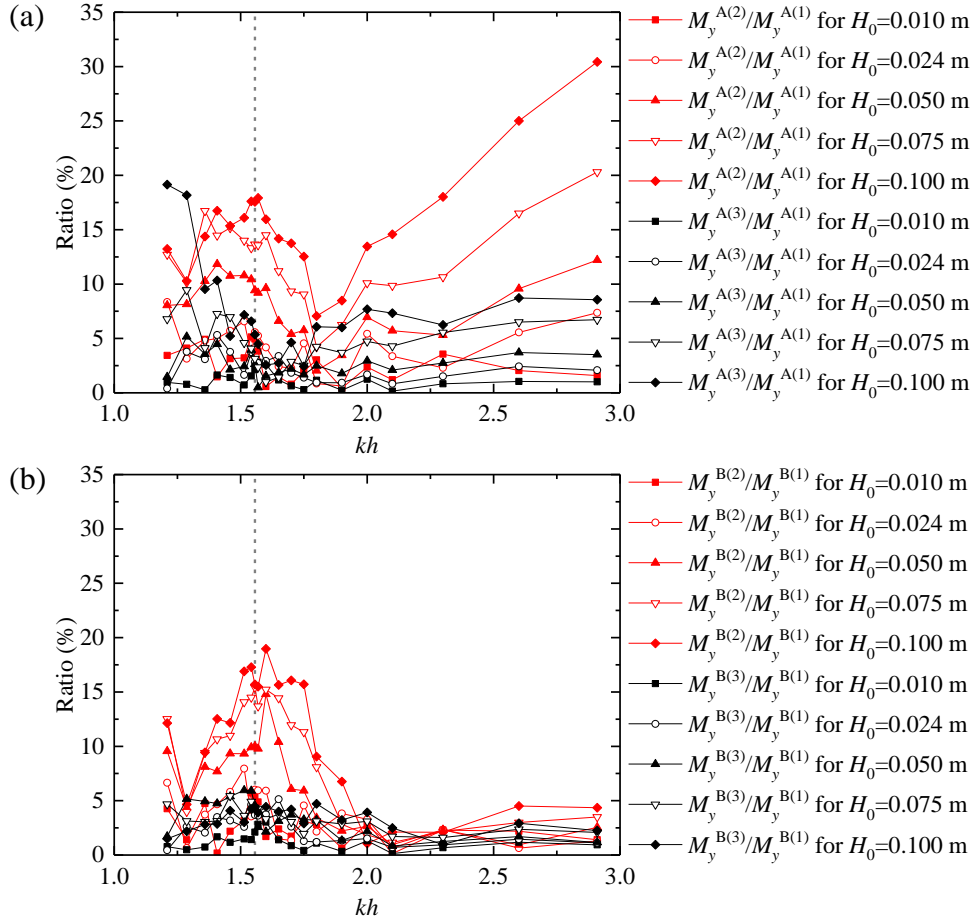
506

507

508

509

Fig. 16. The first three order harmonic components of the moments on Boxes A and B under the conditions of various incident wave heights.



510

511

Fig. 17. Ratios of the second- and third-order harmonic components to the first-order harmonic

512

components for the moments on (a) Box A and (b) Box B under the conditions of various incident

513

wave heights

514

515

5.3 Reflection, transmission and energy loss coefficients

516

Based on the wave analysis technique in [Goda and Suzuki \(1976\)](#), the wave height of the

517

reflected waves from the two-box system can be obtained by using the free-surface elevations at G_1

518

and G_2 (refer to Fig. 1). The reflection coefficient C_r is further calculated as the ratio of the reflected

519

wave height to the incident wave height H_0 . The transmission coefficient C_t is defined as the ratio

520

of the transmitted wave height to H_0 , and the transmitted wave height can be obtained by the free-

521

surface elevation at G_4 . Then, the energy loss coefficient $L_e = 1 - C_r^2 - C_t^2$ is calculated. The effects

522

of the incident wave height on the reflection, transmission and energy loss coefficients, C_r , C_t and

523

L_e , are illustrated in Fig. 18. For the reflection coefficient (Fig. 18a), the following three phenomena

524

can be easily observed. First, the reflection coefficients C_r near the resonant frequency are always

525 less than those away from the resonant frequency. Second, the reflection coefficient at the resonant
526 frequency increases with the increasing of the incident wave height. Third, under the conditions of
527 $H_0=0.050$ m and 0.075 m, both the two variation curves of the reflection coefficient around the
528 resonant frequency almost become flat, which indicates that the similar wave energy can propagate
529 into the gap. Hence, this leads to the relatively flat variation curves of H_g/H_0 around the resonant
530 frequency for $H_0=0.050$ m and 0.075 m shown in Fig. 8a.

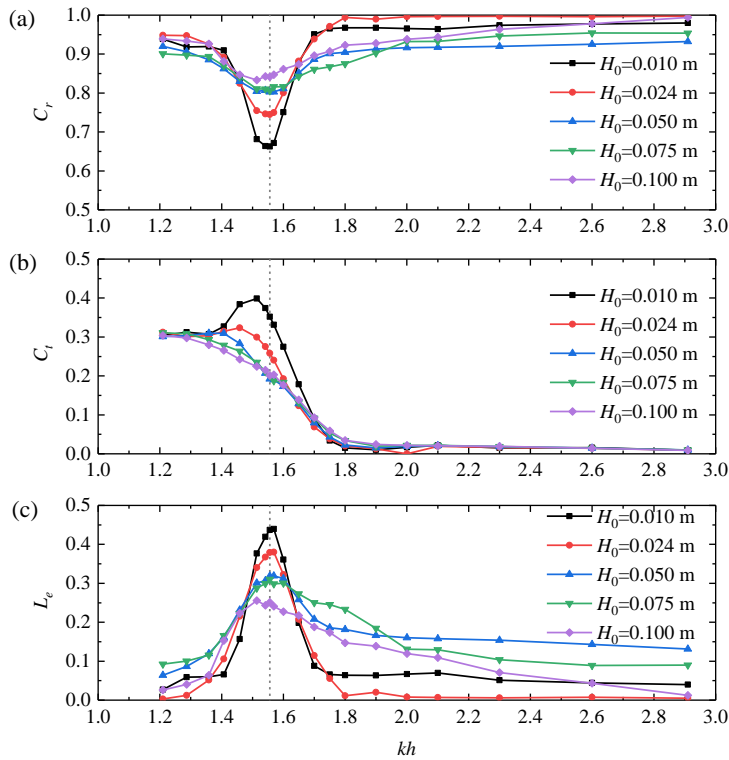
531 For the transmission coefficient (Fig. 18b), the frequency at which the maximum transmission
532 coefficient C_t occurs is always less than the resonant frequency. The larger the incident wave height
533 is, the more obvious their difference becomes. When the incident wave height is small, the
534 transmission coefficient first increases, then sharply decreases, then slowly increases, and then
535 slowly decreases with the non-dimensional wavenumber, kh . However, with the increase of the
536 incident wave height, the vertical wave forces gradually become monotonic decrease with kh . These
537 effects of the incident wave height on the variation characteristics of the transmission coefficient
538 are very similar to its effects on those of the vertical wave forces on Boxes A and B (see Fig. 8b and
539 c).

540 By carefully comparing Fig. 18a and b, it can be found that for all the incident wave heights
541 considered in this paper, the reflection coefficients are always larger than the transmission
542 coefficient, no matter whether the gap resonance occurs or not. The larger the incident wave height
543 is, the more obvious the difference between C_r and C_t becomes. This explains that phenomenon
544 shown in Fig. 8d and e that for the horizontal wave forces on Box A, the frequency at which the
545 maximum horizontal force occurs obviously deviates from the resonant frequency; while for the
546 horizontal wave forces on Box B, the frequency at which the maximum horizontal force occurs is
547 approximately equal to the resonant frequency.

548 For the energy loss coefficient (Fig. 18c), it is seen that for all the incident wave heights
549 considered in this paper, almost all the maximum energy loss coefficients appear at (or very close
550 to) the resonant frequency. Besides, with the increase of the incident wave height, the energy loss
551 coefficient at the resonant frequency becomes smaller and smaller. It should be noted that, intuitively,
552 this finding seems to be incompatible with that phenomenon shown in Fig. 8a that larger incident
553 wave height leads to smaller amplification of the free-surface elevation in the gap. In fact, these two
554 findings are compatible with each other. The reason lies on that the increase of the incident wave

555 height tends to remarkably augment the reflection coefficient at the resonant frequency, and hence
 556 relatively less wave energy can propagate into the gap. Therefore, less energy dissipation and
 557 smaller free-surface amplification in the narrow gap can be observed at the resonant frequency,
 558 which agrees with the related findings in [Jiang et al. \(2018\)](#).

559



560
 561 **Fig. 18.** Variations of (a) the reflection coefficient, (b) the transmission coefficient and (c) the energy
 562 loss coefficient with respect to the wave frequency under the conditions of various incident wave
 563 heights

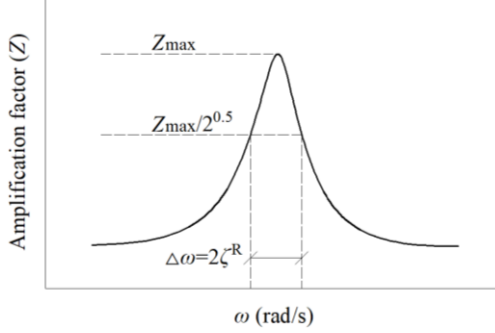
564

565 5.4 Response time and damping time of gap resonance

566 In practical engineering applications, the fast and accurate estimation of the response time and
 567 the damping time is crucial for the safe evacuation of staff and the reasonable arrangement of
 568 operation time during the offloading operations from FPSO platforms to a shuttle tanker under gap
 569 resonance conditions. In this section, a general method is proposed for accurately estimating both
 570 the response time and the damping time of free-surface elevation in the gap under resonance. The
 571 general method is based on fitting the envelope of the free-surface elevation. For the evaluation of
 572 the response time, there is an alternative method which is based on the amplification curve of the

573 free-surface elevation in the gap.

574



575

576

577

Fig. 19. Generic amplification curve; $\Delta\omega$ is the half-power spectral bandwidth

578

579

580

581

582

583

584

585

586

These methods are inspired by [Bellotti \(2007\)](#) and [Dong et al. \(2010\)](#) who investigated the response time and the damping time of the harbor to long waves under the condition of harbor resonance. In order to facilitate the understanding of the reader, the basic principle of these methods is briefly explained here. To illustrate the basic principle, Fig. 19 shows a generic amplification curve, in which Z is the amplification factor. The free-surface elevation in the narrow gap can be considered as typical of a 1D system like a mass-spring system, moving along a line, connected to a damper, forced by a periodically unit force. If the considered mass starts from rest (i.e., from the position $z=0$), when the frequency of the force equals the natural frequency of the system, its position along the axis (z) can be formulated as

587

$$z = Z_{\max} \cos(-\omega \cdot t^*) (1 - e^{-\zeta^R \cdot t^*}), \quad (7)$$

588

589

590

591

in which ζ^R is a parameter governing the response time of the resonator, Z_{\max} is the maximum amplification factor and t^* denotes the relative time with respect to the moment that the mass just begins to move from rest. It requires infinite time for the fluctuation to reach its maximum, following Eq. (7). The time $t_{\alpha\%}^*$ needed for the waves to reach $\alpha\%$ of the maximum can be formulated as

592

$$t_{\alpha\%}^* = -\frac{\ln(1-\alpha\%)}{\zeta^R}. \quad (8)$$

593

594

Similarly, if the mass damps from the steady-state maximum to the rest state, its position can be expressed as

595

$$z = Z_{\max} \cos(-\omega \cdot \tau) e^{-\zeta^D \cdot \tau}, \quad (9)$$

596

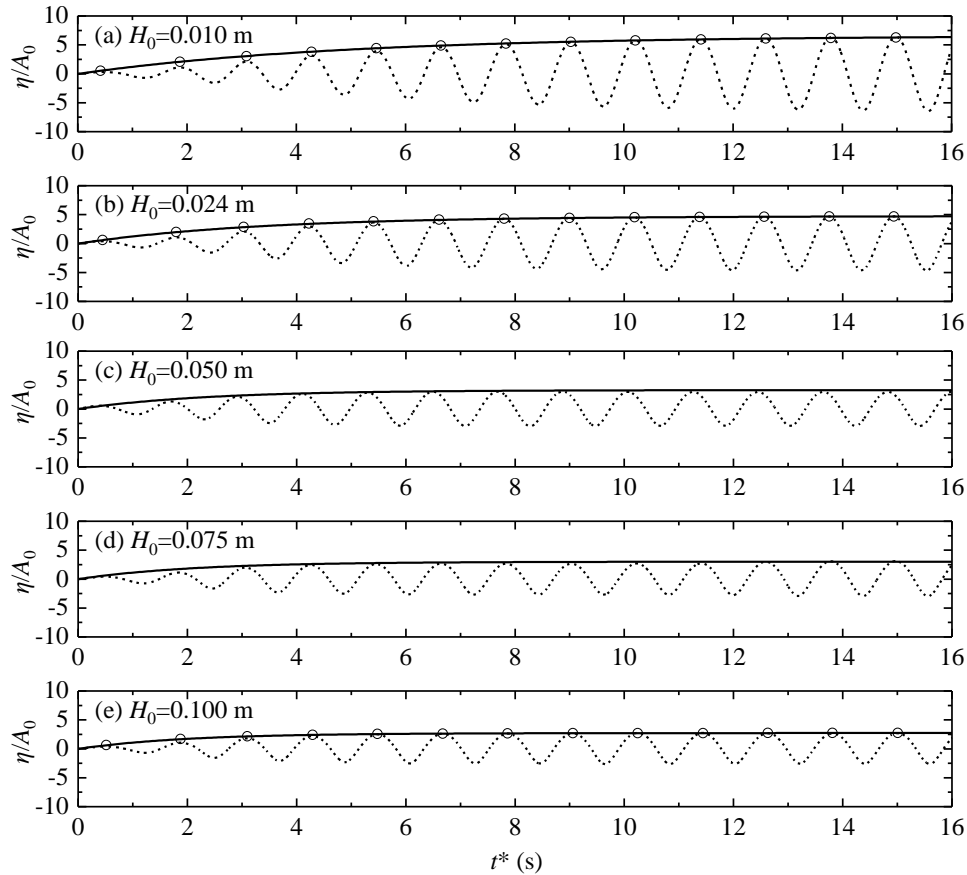
597

where ζ^D is a parameter controlling the damping time of the resonator and τ denotes the relative time with respect to the moment that the mass just begins to damp from the steady-state maximum.

598 The time $\tau_{\beta\%}$ needed by the wave to decrease to $\beta\%$ of the maximum can be expressed as

599
$$\tau_{\beta\%} = -\frac{\ln(\beta\%)}{\zeta^D}. \quad (10)$$

600 It can be found from Eqs. (8) and (10) that the key step to quantitatively evaluate the response
601 time and the damping time lies on how to find the values of ζ^R and ζ^D . A general method to obtain
602 their values is to directly fit the measured (or simulated) envelopes of the displacement of the mass
603 with the theoretical ones formulated by Eqs. (7) and (9). It can be demonstrated that for 1D
604 resonators, the value of ζ^R can also be evaluated from the amplification curve. More specifically,
605 $\zeta^R = \Delta\omega/2$, in which $\Delta\omega$ is the half-power spectral bandwidth (i.e., the width of the part of the
606 amplification curve with values larger than $Z_{\max}/2^{0.5}$). Identical to [Bellotti \(2007\)](#) and [Dong et al.](#)
607 [\(2010\)](#), $t_{95\%}^*$ and $\tau_{5\%}$ are selected in this article to represent the response time and the damping
608 time of the resonant free-surface elevations, respectively.



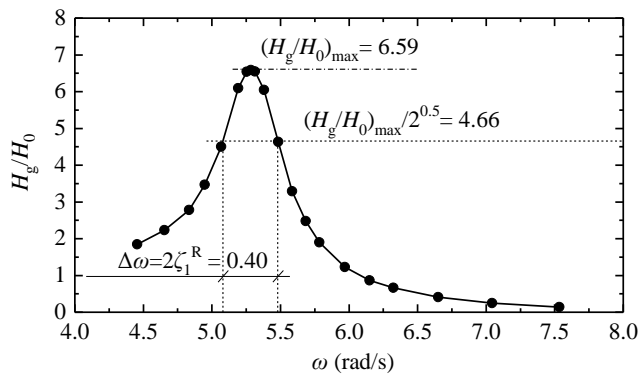
609 **Fig. 20.** The response process of the free-surface elevation (η/A_0) in the narrow gap excited by the
610 incident regular waves with the resonant frequency (i.e., $kh=1.556$, or equivalently $\omega=5.285$ rad/s)
611 and various heights. Dashed lines denote the time histories of the simulated free-surface elevations
612

613 obtain by the numerical model. Solid lines refer to the fitted envelope of η/A_0 obtained by directly
 614 fitting the simulated envelopes with the theoretical ones formulated by Eq. (7). Small circles
 615 represent the envelope of η/A_0 as obtained by Eq. (7) using the amplification curve method for
 616 estimating ζ^R .

617

618 Fig. 20 shows the time histories of the free-surface elevations in the narrow gap, obtained by
 619 using the time-resolving numerical model, from the calm to the steady state. The frequency of all
 620 the incident regular waves corresponds to the resonant frequency (i.e., $kh=1.556$, or equivalently
 621 $\omega=5.285$ rad/s). By directly fitting the simulated envelopes with the theoretical ones formulated by
 622 Eq. (7), the numerical values of ζ^R can be obtained. Besides, by measuring the half-power spectral
 623 bandwidth of the amplification curve as shown in Fig. 19, the values of ζ^R can also be calculated. It
 624 is noted here that, to facilitate comparing the values of ζ^R obtained by these two different methods,
 625 two different symbols, ζ_1^R and ζ_2^R , are used separately to represent the values of ζ^R obtained by the
 626 amplification curve method and by the direct envelope-fitting method in the following. As a
 627 concrete example of employing the amplification curve method to evaluate the value of ζ_1^R , Fig. 21
 628 illustrates the amplification curve of the free-surface elevation in the narrow gap under the condition
 629 of $H_0=0.010$ m. It can be seen that the value of ζ_1^R under the condition of $H_0=0.010$ m is equal to
 630 0.20.

631



632

633 **Fig. 21.** Amplification curve of the free-surface elevation in the narrow gap under the condition of
 634 $H_0=0.010$ m

635 Table 1 further lists all the values of ζ_1^R and ζ_2^R , their relative percentage errors, Err , and

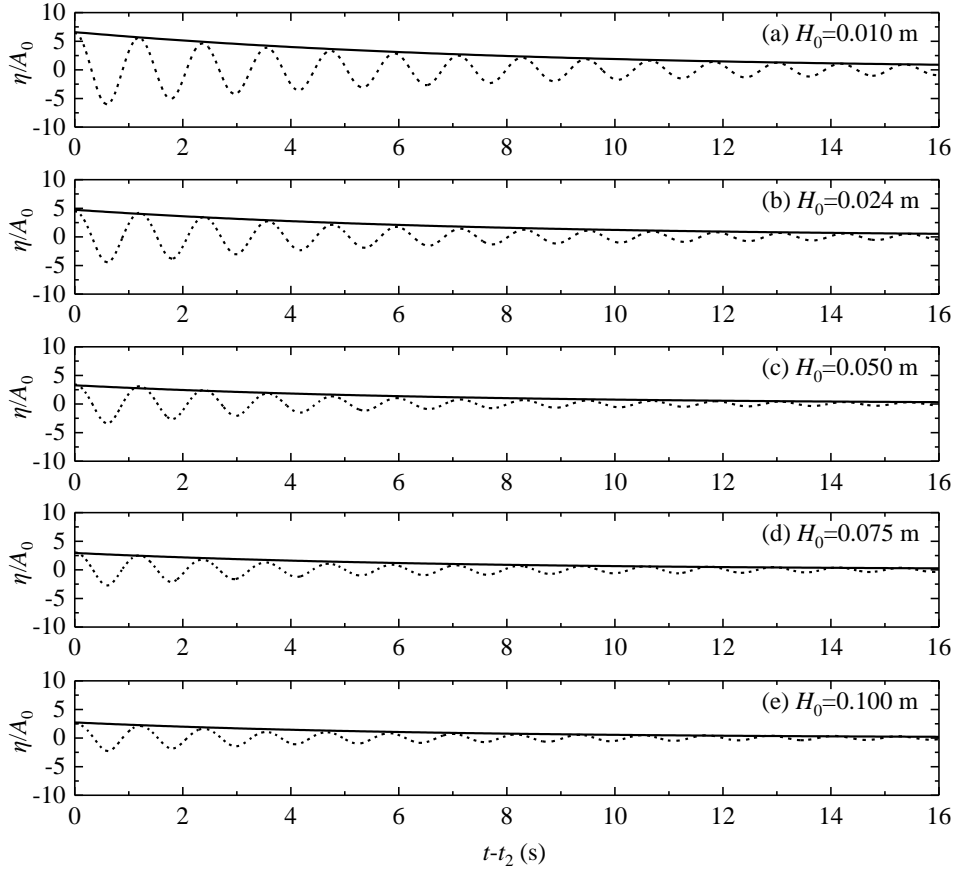
636 the response time, $t_{95\%}^*$ for the free-surface elevations shown in Fig. 20. The response time, $t_{95\%}^*$,
637 in this table is calculated by employing Eq. (8) and the value of ζ_2^R . As mentioned in Section 5.1,
638 unlike the typical amplification curves shown in Figs. 19 and 21, the two free-surface amplification
639 curves for $H_0=0.050$ m and 0.075 m do not present the perfect single-peak shape; the two curves
640 around the resonant frequency become flat, and the values of the amplification factor at $kh=1.556$
641 are even slightly less than the ones at its both adjacent sides (refer to Fig. 8a). Hence, the values of
642 ζ_1^R for $H_0=0.050$ m and 0.075 m are absent. For the other three wave heights, the relative
643 percentage errors between ζ_1^R and ζ_2^R are shown to be extremely small. Besides, observing Fig.
644 20 can easily find that for all the incident wave heights considered in this paper, both the two
645 envelopes of the free-surface elevations obtained by ζ_1^R and ζ_2^R agree well with the corresponding
646 simulated free-surface elevations by using the time-resolving numerical model. These phenomena
647 indicate that both the two above-mentioned methods for evaluating the response time of gap
648 resonance are accurate and reliable.

649
650 **Table 1.** All the parameters related to the response time and the damping time of the resonant free-
651 surface elevations shown in Figs. 20 and 22. *Err* denotes the relative percentage error between ζ_1^R
652 and ζ_2^R . $t_{95\%}^*$ and $\tau_{5\%}$ refers to the response time and the damping time of the free-surface
653 elevations, respectively. The evaluation of $t_{95\%}^*$ is based on Eq. (8) and the value of ζ_2^R .

H_0 (m)	ζ_1^R	ζ_2^R	<i>Err</i> (%)	$t_{95\%}^*$ (s)	ζ^D	$\tau_{5\%}$ (s)	$\tau_{5\%}/t_{95\%}^*$
0.010	0.200	0.202	0.99	14.83	0.125	23.97	1.62
0.024	0.306	0.299	2.34	10.02	0.136	22.03	2.20
0.050	-	0.421	-	7.12	0.145	20.66	2.91
0.075	-	0.467	-	6.41	0.151	19.84	3.09
0.100	0.512	0.499	2.60	6.00	0.158	18.96	3.16

654

655



656

657

658

659

660

661

662

663

664

665

666

667

668

669

670

671

672

Fig. 22. The damping process of the free-surface elevation (η/A_0) in the narrow gap excited by the incident regular waves with the resonant frequency (i.e., $kh=1.556$, or equivalently $\omega=5.285$ rad/s) and various heights. Dashed lines denote the time histories of the simulated free-surface elevations obtain by the numerical model. Solid lines represent the fitted envelope of η/A_0 obtained by directly fitting the simulated envelopes with the theoretical ones formulated by Eq. (9).

Fig. 22 illustrates the time histories of the simulated free-surface elevations in the narrow gap and their fitted envelopes obtained by directly fitting the simulated envelopes with the theoretical ones formulated by Eq. (9) during their damping processes. It is seen that for all the incident wave heights considered in this paper, Eq. (9) can describe the damping process of the resonant free-surface elevation in the gap very well. All the values of ζ^D gained by the direct envelope-fitting method and the damping time $\tau_{5\%}$ under the conditions of various wave heights are also presented in Table 1.

According to the response time and the damping time presented in Table 1, the following two phenomena can be easily observed. First, for all the incident wave heights, the damping time is always significantly larger than the corresponding response time. The ratio of the damping time to

673 the response time gradually increases from 1.62 for $H_0=0.010$ m to 3.16 for $H_0=0.100$ m. This
674 indicates that once the gap resonance is excited, it will persist for a rather long time. Second, both
675 the response time and the damping time decrease with the incident wave height, and the decreasing
676 degree of the response time is obviously larger than that of the damping time. The response time
677 falls up to 60 % from $H_0=0.010$ m to $H_0=0.100$ m, while the damping time reduces only about 21%.

678

679 6. Conclusions

680 The CFD numerical model, OpenFOAM®, together with the wave generation toolbox
681 “waves2Foam” proposed by [Jacobsen et al. \(2012\)](#), is adopted for investigating the hydrodynamic
682 behaviors of water resonance in a narrow gap formed by two side-by-side identical boxes excited
683 by incident regular waves with various wave heights. The overall free-surface amplification in the
684 gap and the overall wave loads on the boxes are firstly presented. Then, the harmonic analyses of
685 free-surface elevation and wave loads are mainly investigated. Next, the reflection, transmission
686 and energy loss coefficients of the two-box system are discussed. Finally, two different methods to
687 evaluate the response time and the damping time of gap resonance are proposed. The results of this
688 study have provided new insights of the hydrodynamic characteristics involved in the gap resonance.

689 The following conclusions can be drawn from the results of the present study:

- 690 (1) The frequencies at which the maximum vertical wave forces on both boxes and the maximum
691 horizontal wave force on Box A occur appear to obviously deviate from the resonant frequency,
692 and a larger incident wave height tends to cause more obvious differences between them. While
693 the frequency at which the maximum horizontal force on Box B occurs is equal or very close
694 to the resonant frequency.
- 695 (2) For the free-surface elevation in the gap and the moments on boxes, the ratios of their second-
696 order components to the corresponding first-order ones around the resonant frequency are
697 normally larger than those at the frequencies far from the resonant frequency (except those at
698 the very high frequency band). The larger the incident wave height is, the larger the ratios of
699 the second- to the first-order components around the resonant frequency becomes.
- 700 (3) For both the vertical and horizontal wave forces on both boxes, the ratios of their second- to the
701 first-order components near the resonant frequency are less than those far away from the
702 resonant frequency. Besides, when the incident wave height is small, their second-order

703 components are obviously larger than the corresponding third-order ones around the resonant
704 frequency. However, as the incident wave height increases, the third-order components around
705 the resonant frequency gradually approach and even exceed the second-order ones.

706 (4) Both the minimum reflection coefficient and the maximum energy loss coefficient always
707 appear at (or very close to) the resonant frequency, while the frequency at which the maximum
708 transmission coefficient appears is obvious less than the resonant frequency. The reflection
709 coefficient is always larger than the transmission coefficient, and the larger the incident wave
710 height is, the more obvious their difference becomes. Besides, the energy loss coefficient under
711 the gap resonance condition gradually decreases with the increase of the incident wave height.

712 (5) Both the amplification curve method and the direct envelope-fitting method are able to
713 accurately evaluate the response time and the damping time of the resonant free-surface
714 elevation in the gap, and it is shown that the damping time is always significantly larger than
715 the corresponding response time. Besides, with the increase of the incident wave height, both
716 the response time and the damping time decrease, and the decreasing degree of the former is
717 obviously larger than that of the latter.

718 **Finally, we reaffirm here that these conclusions are only valid for the given geometric layout**
719 **(including the size and draft of the two boxes, the gap width and the water depth) and the ranges of**
720 **the incident wave height and the incident wave frequency studied in this paper.**

721

722 **Acknowledgments**

723 This work is financially supported by the National Natural Science Foundation of China (Grant
724 no. 51609108) and the Jiangsu Government Scholarship for Overseas Studies (awarded to Dr.
725 Junliang Gao for study abroad at the University of Bath). The authors also thank UK EPSRC and
726 the Royal Academy of Engineering for providing partial support for this work within the UK-China
727 joint projects ResIn (EPSRC Grant No. EP/R007519/1) and the UK-CIAPP (RAE Grant No. UK-
728 CIAPP/73). We also express our thanks to Dr. Wei Bai (Manchester Metropolitan University) and
729 Dr. Xingya Feng (University of Oxford) for their support for this study.

730

731 **References**

732 Bellotti, G., 2007. Transient response of harbours to long waves under resonance conditions. Coastal
733 Engineering 54 (9), 680-693.

734 Chen, X.B., 2004. Hydrodynamics in Offshore and Naval Applications (Keynote lecture), The 6th
735 International Conference on Hydrodynamics, Perth, Australia.

736 Dong, G., Wang, G., Ma, X., Ma, Y., 2010. Numerical study of transient nonlinear harbor resonance.
737 Science China-Technological Sciences 53, 558-565.

738 Feng, X., Bai, W., Chen, X.B., Qian, L., Ma, Z.H., 2017. Numerical investigation of viscous effects
739 on the gap resonance between side-by-side barges. Ocean Engineering 145, 44-58.

740 Goda, Y., Suzuki, T., 1976. Estimation of incident and reflected waves in random wave experiments,
741 Proceedings of the 15th Coastal Engineering Conference, Honolulu, Hawaii, pp. 828-845.

742 Huijsmans, R.H.M., Pinkster, J.A., Wilde, J.J.d., 2001. Diffraction and radiation of waves around
743 side-by-side moored vessels, Proceedings of the Eleventh (2001) International Offshore and
744 Polar Engineering Conference, Stavanger, Norway.

745 Iwata, H., Saitoh, T., Miao, G., 2007. Fluid resonance in narrow gaps of very large floating structure
746 composed of rectangular modules, Proceedings of the 4th International Conference on Asian
747 and Pacific Coasts, Nanjing, China, pp. 815-826.

748 Jacobsen, N.G., Fuhrman, D.R., Fredsøe, J., 2012. A wave generation toolbox for the open-source
749 CFD library: OpenFoam®. International Journal for Numerical Methods in Fluids 70 (9), 1073-
750 1088.

751 Jiang, S.-C., Bai, W., Tang, G.-Q., 2018. Numerical simulation of wave resonance in the narrow gap
752 between two non-identical boxes. Ocean Engineering 156, 38-60.

753 Li, B., Cheng, L., J.Deeks, A., BinTeng, 2005. A modified scaled boundary finite-element method
754 for problems with parallel side-faces. Part II. Application and evaluation. Applied Ocean
755 Research 27 (4-5), 224-234.

756 Li, Y., Zhang, C., 2016. Analysis of wave resonance in gap between two heaving barges. Ocean
757 Engineering 117, 210-220.

758 Lu, L., Chen, L., Teng, B., Zhao, M., 2010a. Numerical investigation of fluid resonance in two
759 narrow gaps of three identical rectangular structures. Applied Ocean Research 32 177-190.

760 Lu, L., Cheng, L., Teng, B., Sun, L., 2010b. Numerical simulation and comparison of potential flow
761 and viscous fluid models in near trapping of narrow gaps. Journal of Hydrodynamics, Ser. B

762 22 (5), 120-125.

763 Lu, L., Teng, B., Cheng, L., Li, Y., 2008. Numerical simulation of hydrodynamic resonance in a
764 narrow gap between twin bodies subject to water waves, The Eighteenth International Offshore
765 and Polar Engineering Conference, Vancouver, Canada.

766 Lu, L., Teng, B., Cheng, L., Sun, L., Chen, X., 2011a. Modelling of multi-bodies in close proximity
767 under water waves—Fluid resonance in narrow gaps. *Science China Physics, Mechanics and
768 Astronomy* 54 (1), 16-25.

769 Lu, L., Teng, B., Sun, L., Chen, B., 2011b. Modelling of multi-bodies in close proximity under water
770 waves—Fluid forces on floating bodies. *Ocean Engineering* 38 (13), 1403-1416.

771 Mavrakos, S.A., Chatjigeorgiou, I.K., 2009. Second-order hydrodynamic effects on an arrangement
772 of two concentric truncated vertical cylinders. *Marine Structures* 22 (3), 545-575.

773 Miao, G., Ishida, H., Saitoh, T., 2000. Influence of gaps between multiple floating bodies on wave
774 forces. *China Ocean Engineering* 14 (4), 407-422.

775 Molin, B., 2001. On the piston and sloshing modes in moonpools. *Journal of Fluid Mechanics* 430,
776 27-50.

777 Moradi, N., Zhou, T., Cheng, L., 2015. Effect of inlet configuration on wave resonance in the narrow
778 gap of two fixed bodies in close proximity. *Ocean Engineering* 103 88-102.

779 Moradi, N., Zhou, T., Cheng, L., 2016. Two-dimensional numerical study on the effect of water
780 depth on resonance behaviour of the fluid trapped between two side-by-side bodies. *Applied
781 Ocean Research* 58, 218-231.

782 Newman, J.N., 2004. Progress in wave load computations on offshore structures (Invited lecture),
783 The 23th Conference on Offshore Mechanics and Arctic Engineering (OMAE2004), New York,
784 USA.

785 Ning, D., Su, X., Zhao, M., Teng, B., 2015a. Hydrodynamic difference of rectangular-box systems
786 with and without narrow gaps. *Journal of Engineering Mechanics* 141 (8), 04015023.

787 Ning, D., Su, X., Zhao, M., Teng, B., 2015b. Numerical study of resonance induced by wave action
788 on multiple rectangular boxes with narrow gaps. *Acta Oceanologica Sinica* 34 (5), 92-102.

789 Pauw, W.H., H.M.Huijsmans, R., Voogt, A., 2007. Advances in the Hydrodynamics of Side-by-Side
790 Moored Vessels, Proceedings of the 26th International Conference on Offshore Mechanics and
791 Arctic Engineering (OMAE2017), San Diego, California, USA.

792 Rodríguez, M., Spinneken, J., 2016. A laboratory study on the loading and motion of a heaving box.
793 Journal of Fluids and Structures 64, 107-126.

794 Saitoh, T., Miao, G., Ishida, H., 2006. Theoretical analysis on appearance condition of fluid
795 resonance in a narrow gap between two modules of very large floating structure, Proceedings
796 of the 3rd Asia-Pacific Workshop on Marine Hydrodynamics, Shanghai, China, pp. 170-175.

797 Sun, L., Taylor, R.E., Taylor, P.H., 2010. First- and second-order analysis of resonant waves between
798 adjacent barges. Journal of Fluids and Structures 26 (6), 954-978.

799 Tan, L., Lu, L., Liu, Y., Sabodash, O.A., Teng, B., 2014. Dissipative Effects of Resonant Waves in
800 Confined Space Formed by Floating Box in Front of Vertical Wall, The Eleventh ISOPE
801 Pacific/Asia Offshore Mechanics Symposium, Shanghai, China

802 Zhao, W., Wolgamot, H.A., Taylor, P.H., Taylor, R.E., 2017. Gap resonance and higher harmonics
803 driven by focused transient wave groups. Journal of Fluid Mechanics 812, 905-939.

804